Inorganic Chemistry

pubs.acs.org/IC Article

The Deep Eutectic Solvent Precipitation Synthesis of Metastable $Zn_4V_2O_9$

Sangki Hong, Ye Cheng, Shruti Hariyani, Jingzhe Li, Rachel M. Doughty, Aishwarya Mantravadi, Adedoyin N. Adeyemi, Emily A. Smith, Jakoah Brgoch, Frank E. Osterloh, and Julia V. Zaikina*

Cite This: *Inorg. Chem.* 2022, 61, 154−169 Read Online

ACCESS | Metrics & More | Article Recommendations | Supporting Information

ABSTRACT: A precipitation method involving a deep eutectic solvent (DES)—a mixture of hydrogen bond donor and acceptor—is used to synthesize a ternary metal oxide. Without toxic reagents, precipitates consisting of $Zn_3(OH)_2V_2O_7{\cdot}nH_2O$ and $Zn_5(OH)_6(CO_3)_2$ are obtained by simply introducing deionized H_2O to the DES solution containing dissolved ZnO and V_2O_5. Manipulation of the synthetic conditions demonstrates high tunability in the size/morphology of the two-dimensional nanosheets precipitated during the dynamic equilibrium process. According to differential scanning calorimetry and high-temperature powder X-ray diffraction, $Zn_3V_2O_8$ and ZnO obtained by the annealing of the precipitate are intermediates in the reaction pathway toward metastable $Zn_4V_2O_9$. Intimate mixing of the metal precursors achieved by the precipitation method allows access to the metastable zinc-rich vanadate with unusually rapid heat treatment. The UV−vis and surface photovoltage spectra reveal the presence of sub-band gap states, stemming from the reduced vanadium (V^{4+}) center. Photoelectrochemical measurements confirm weak photoanodic currents for water and methanol oxidation. For the first time, this work shows the synthesis of a metastable oxide with the DES-precipitation route and provides insight into the structure−property relationship of the zinc-rich vanadate.

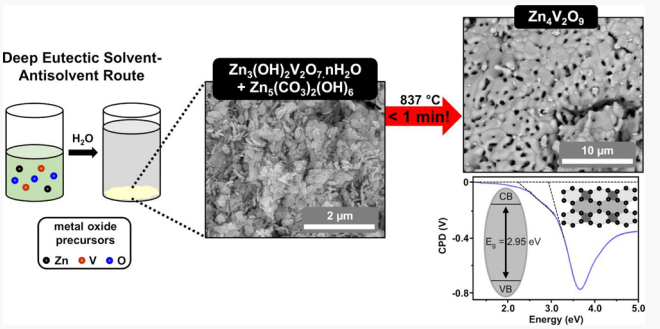

1. INTRODUCTION

Metastable materials, which lie at the local minima of energy landscape, expand our understanding of structure and property relationships. Density functional theory (DFT), together with large material databases such as Open Quantum Materials Database (OQMD)[1] and Inorganic Crystal Structure Database (ICSD),[2,3] allows for high-throughput discovery of new metastable compounds above the convex hull of chemical space.[4] However, computational predictions have gone beyond experimental synthetic ability. Although identifying the thermodynamic upper limit in the energy scale helps determine which materials are synthesizable,[5,6] the evaluation of various synthetic parameters toward synthesizability is currently unavailable in computational methods. Conspicuous efforts with a variety of synthetic techniques have been made to access metastable materials. For instance, high-pressure synthesis was utilized to prepare multiferroic $BiMnO_3$.[7] A potential solar cell absorber β-$CuGaO_2$, a low-dimensional magnet Cu_4O_3, and an oxygen evolution photocatalyst $(Ba_{0.6}Sn_{0.4})(Zr_{0.5}Ti_{0.5})O_3$ can be prepared by the ion-exchange reaction, solvothermal route, and flux-assisted method using $SnCl_2/SnF_2$ peritectic flux, respectively.[8−10] The chemical precipitation method is another way of achieving metastable compounds. Preparation of hexagonal MoO_3 was realized by utilizing concentrated HCl solution as a precipitation agent.[11] Similarly, introducing ammonia solution into the metal precursor is the key step in the synthesis of tetragonal NiO-ZrO_2 solid solution.[12] In addition, a mild reaction temperature (<100 °C) and attainable scale-up are recognized as advantages of the precipitation route.[13−15]

Deep eutectic solvents (DESs) are an emerging class of materials made by mixing a hydrogen bond donor and acceptor. The eutectic mixture of the constituents promotes significant melting point depression through hydrogen bonding.[16−19] Importantly, the resulting viscous liquid holds strong solvation capability of various metal precursors, including binary oxides and metal salts, featuring DESs as suitable reaction media in the preparation of functional metal oxides.[20−25] A combustion reaction involving metal precursors thoroughly mixed in the desired ratio in DESs allows for control over the metal composition and particle size of the oxides.[20−25] We have previously shown that such a route can be used to synthesize oxygen vacancy containing $M_2V_2O_7$ and

Received: August 16, 2021
Published: December 13, 2021

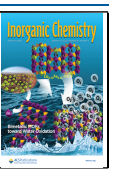

https://doi.org/10.1021/acs.inorgchem.1c02511
Inorg. Chem. 2022, 61, 154−169

MV_2O_6 (M = Cu or Zn) by controlling M:V ratios in DES and optimizing the heating profile.[23,24] Furthermore, as a "designer solvent", DESs provide synthetic tunability through a number of different combinations of hydrogen bond donor and acceptor, leading to a variety of accessible metal oxides.[20−27] The versatility of DESs in oxide material syntheses has been further demonstrated by implementing the precipitation route. Without the use of toxic reagents such as strong acid and base, size/morphology-tunable binary metal oxides ZnO are achieved.[28−31] Considering the simplicity of the experimental procedure and the significant number of synthetic variables available to work with, the DES-involved precipitation route can provide opportunities for new oxide material discovery.

With the depletion of fossil fuels and their negative impact on our environments, the development of new technology to reduce energy consumption/CO_2 emission and ultimately make use of sustainable fuel has become an urgent need. As a part of the eco-friendly movement, numerous efforts have been made to develop efficient semiconducting metal oxide materials for energy-related applications. For instance, zinc-rich vanadates have been identified as a potential anode material for lithium-ion batteries (energy storage).[32−34] Excellent rate performance, cycling stability, and high discharge capacity were reported for both $Zn_3V_2O_8$ and $Zn_3(OH)_2V_2O_7\cdot 2H_2O$).[33,34] In addition to the energy storage, $Zn_3V_2O_8$ has shown reasonable light-harvesting property—a quantum yield of 0.64% with a photocatalytic oxygen evolution reaction (OER) rate of 10.2 μmol/h under visible light ($\lambda \geq 420$ nm) from a silver nitrate solution.[35] Several vanadium oxides have been identified as potential phosphor material in white light-emitting diodes (LEDs).[36−40] An intense broad-band emission from 380 to ∼800 nm with internal quantum efficiencies of 79% and 87% was reported for $RbVO_3$ and $CsVO_3$, respectively.[36,37] Zinc-rich compounds in the ZnO-V_2O_5 system have shown to exhibit strong yellow (560 nm) luminescence.[40] In addition, some vanadium oxides have shown good light-harvesting properties, suitable for sustainable chemical fuel production via photoelectrochemical (PEC) water splitting.[41−43] Monoclinic $BiVO_4$ (band gap, ∼2.4 eV) exhibits a quantum yield of 9% with a photocatalytic oxygen evolution reaction (OER) rate of 421 μmol/h under visible light (>420 nm) from a silver nitrate solution.[41] β-$Mn_2V_2O_7$ is another solar light absorber, possessing a band gap of 1.75 eV and suitable band alignment for both OER and the hydrogen evolution reaction (HER).[42] The most zinc-rich vanadate $Zn_4V_2O_9$, however, has never been investigated for its material properties due to synthetic challenge. Here, we report an inimitable DES-involved precipitation synthesis route and properties of a metastable zinc-rich vanadate $Zn_4V_2O_9$. We also discuss the reaction pathway and metastability of the zinc-rich compound. Finally, the electronic structure, optical absorption, vibrational properties, luminescence, surface photovoltage, and PEC characteristics of the compound are evaluated with various experimental and theoretical techniques.

2. EXPERIMENTAL SECTION

2.1. Material Synthesis. ZnO (Alfa, 99.9%), V_2O_5 (Alfa, 99.6% min), and urea (Alfa, 99%, crystalline) were used without purification. Choline chloride (Sigma-Aldrich, ≥98%) was dried under vacuum at 120 °C before the synthesis. A deep eutectic solvent (DES) was prepared by combining urea and choline chloride in a 2:1 molar ratio (54.322 g of urea and 63.750 g of choline chloride) in a Parafilm-covered glass beaker. The mixture was heated at 70 °C with stirring until a clear viscous liquid was obtained. The binary metal oxides (0.567 g of ZnO and 0.633 g of V_2O_5 for Zn:V = 1:1) were then dissolved in the solvent at 70 °C under vigorous stirring. For the various Zn:V ratios (2:1, 1.5:1, 1:1, and 1:2), the mass of V_2O_5 dissolved in the solvent was the same, but different amounts of ZnO were dissolved. Ninety milliliters of deionized (DI) water (0, 25, and 70 °C) was added to 10 g of the precursor-containing solution, which was kept at 70 °C with stirring. For a fast addition, DI water was poured all at once with vigorous stirring. DI water was added dropwise over a span of 3 h using a burette without stirring for a slow addition. After water was added, the reaction mixture was left without stirring at room temperature for 1 day. The resulting precipitates were decanted and washed three times with DI water, followed by drying at 65 °C. For the synthesis of ZnO/$Zn_3V_2O_8$ and $Zn_4V_2O_9$, the dried precipitate was heated at 400 °C for 6 h and 837 °C for 30 s, respectively. About 43 mg of light-yellow powders (ZnO/$Zn_3V_2O_8$ and $Zn_4V_2O_9$ each) was obtained from the precursor solution with a Zn:V ratio of 1:1 and used for all the characterizations, unless otherwise noted. All heat treatments were performed with a heating rate of 10 °C/min in a fused quartz boat in air using a muffle furnace (box-type).

2.2. Characterization. *2.2.1. Powder X-ray Diffraction.* Synthesized samples were inspected by powder X-ray diffraction (PXRD) using a Rigaku Miniflex 600 diffractometer with Cu Kα radiation (λ = 1.54051 Å) and Ni Kβ filter. Diffraction scans were collected on a zero-background plate at room temperature in air. PDXL software with the PDF-2 database was used for phase analysis.[44]

2.2.2. In Situ High-Temperature Synchrotron Powder X-ray Diffraction. High-temperature synchrotron powder X-ray diffraction (HT-PXRD) scans were collected at the 17-BM beamline at the Advanced Photon Source (APS), Argonne National Laboratory (ANL), with average wavelengths λ = 0.24158 and 0.24117 Å for the precipitate (from the precursor solution with Zn:V = 1.5:1) and as-synthesized $Zn_4V_2O_9$, respectively. The powder samples described in Section 2.1 were loaded into a silica capillary with 0.5 mm inner diameter and 0.7 mm outer diameter. Then, the sample-filled capillary was placed into a secondary shield capillary (0.9 mm inner diameter and 1.1 mm outer diameter) and further mounted in a flow furnace. A thermocouple was set as close as possible to the sealed end of the inner silica capillary, and the gas mixture (20% oxygen gas in helium gas) flowed into the open end of the inner capillary during the measurement. Details of the experimental setup can be found elsewhere.[45] The experiment was conducted in the temperature range from 23 to 900 °C. For the precipitate, heating rates of 50 and 10 °C/min up to 200 and 900 °C, respectively, were employed with a cooling rate of 20 °C/min. For the as-synthesized $Zn_4V_2O_9$, a heating/cooling rate of 10 °C/min was used. Rietveld refinements were performed using GSAS software.[46]

2.2.3. Differential Scanning Calorimetry (DSC) and Thermogravimetric Analysis (TGA). The DSC/TGA experiment was performed using a Netzsch STA449 F1 Jupiter coupled with a Netzsch quadrupole mass spectrometer 403 D Aeolos and a Bruker Tensor 37 FTIR spectrometer. Five milligrams of the precipitate powder (from the precursor solution with Zn:V = 1:2) was loaded into a pan-type alumina (Al_2O_3) crucible with an alumina cover. The sample was heated from 40 to 850 °C and subsequently cooled to 282 °C with a rate of 10 °C/min under a constant flow of synthetic air (20% O_2 and 80% N_2).

2.2.4. Scanning Electron Microscopy and Energy Dispersive Spectroscopy. Scanning electron microscopy (SEM) was carried out using a FEI Quanta 250 field emission scanning electron microscope at 15 kV. Elemental composition analysis was performed with energy dispersive X-ray spectroscopy (EDS) by means of an Oxford X-Max 80 detector. Powder samples were deposited on a carbon-taped SEM sample holder, followed by coating with 5 nm iridium metal.

2.2.5. X-ray Photoelectron Spectroscopy (XPS). A Kratos Amicus/ESCA 3400 instrument was used for XPS measurements. Samples were irradiated using Mg Kα X-rays (240 W nonmonochromated) with the pass energy set at 150 eV. Photoelectrons emitted at 0° from the surface normal were energy-analyzed with a DuPont type analyzer.

https://doi.org/10.1021/acs.inorgchem.1c02511
Inorg. Chem. 2022, 61, 154−169

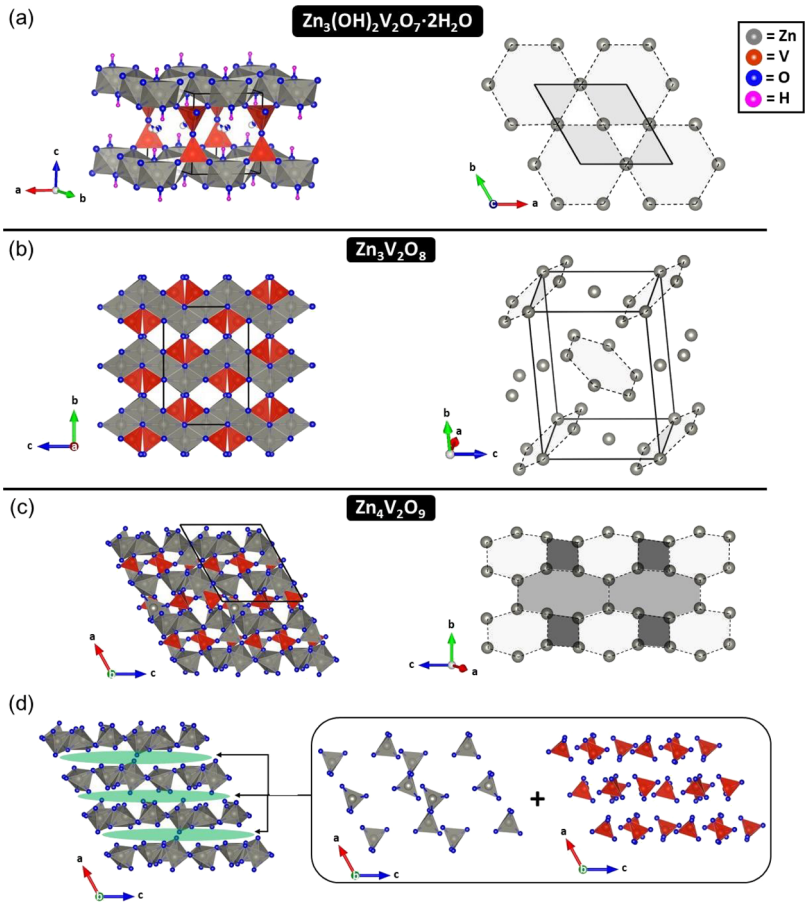

Figure 1. Crystal structures of (a) $Zn_3(OH)_2V_2O_7{\cdot}2H_2O$, (b) $Zn_3V_2O_8$, and (c, d) $Zn_4V_2O_9$. Gray spheres in the figures to the right indicate positions of Zn atoms (a–c).

CasaXPS was used for the processing of raw data files, and a Shirley baseline was applied to all spectra. The charge correction of XPS spectra was made by setting the adventitious C 1s peak to a binding energy of 284.8 eV. XPS data of V_2O_5 (Alfa, 99.99%) was also collected as a reference.

2.2.6. Raman Spectroscopy. An XploRA confocal Raman microscope (HORIBA Scientific, Edison, NJ) was used with a 532 nm laser operating at 1.3 mW. All samples were placed directly onto a coverslip directly and a 50× objective (0.5 NA) was used. Three randomly selected locations were checked for each sample with a 30 s acquisition and three accumulations. The spectra were averaged and plotted in Origin.

2.2.7. FTIR Spectroscopy. Samples were measured in air using attenuated total reflectance Fourier transform infrared spectroscopy (ATR-FTIR). The spectra were collected on a Bruker Tensor 37 using an IRIS germanium ATR accessory from PIKE Industries. The powdered samples were deposited on a germanium crystal and pressed with a clamp. Atmospheric and baseline corrections were applied to all spectra.

2.2.8. Density Functional Theory (DFT) Calculations. First-principles calculations on $Zn_4V_2O_9$ were performed using *ab initio* density functional theory (DFT) as implemented in the Vienna *ab initio* Simulation Package (VASP).[47] All calculations employed a plane-wave basis set with projector-augmented wave (PAW) pseudopotentials.[48] The electronic structure of $Zn_4V_2O_9$ was calculated by using the Heyd–Scuseria–Ernzerhof screen hybrid exchange and correlation functional HSE06, which implements a 75%:25% mixture of the Perdew–Burke–Ernzerhof (PBE):Hartree Fock functionals with a range separation of 0.2 Å.[49] The electronic convergence criterion and ionic convergence criterion were set to 1×10^{-8} eV and 1×10^{-6} eV/Å, respectively. An energy cutoff of 500 eV was used and the first Brillouin zone was described by a Monkhorst–Pack *k*-point grid of 4 × 6 × 6 or ∼1000 *k*-points/atom.[50] Phonon dispersion curves were calculated using the modified Parlinski–Li–Kawazoe *ab initio* force constant method as detailed in the PHONOPY package.[51] The phonons at the Γ-point and macroscopic dielectric tensor were necessary to calculate the Raman spectrum of $Zn_4V_2O_9$ according to the open source code vasp_raman.py made available by Fonari and Stauffer.[52]

2.2.9. Photoluminescence (PL) Spectroscopy. Optical characterization was conducted by mixing the obtained powder in an optically transparent resin (GE Silicones, RTV615) and depositing the mixture on a quartz slide (Chemglass). $Zn_4V_2O_9$ was screened for photoluminescence using a PTI fluorescence spectrophotometer with a 75 W xenon arc lamp for excitation and a Horiba Fluoromax-4 fluorescence spectrophotometer with a 150 W xenon arc lamp for excitation. A Janis cryostat (VPF-100) was also employed for luminescence measurements at 77 K.

2.2.10. Diffuse Reflectance UV–vis Spectroscopy. The diffuse reflectance UV–vis absorption spectrum was collected using an SL1 tungsten halogen lamp (visIR), a SL3 deuterium lamp (UV), and a BLACK-Comet C-SR-100 spectrometer. Flattened and compressed powder samples were prepared on a glass slide for the measurement. A band gap value was estimated with a Tauc method by plotting $(\mathrm{Abs} \times h\nu)^{1/r}$ vs $h\nu$, where Abs is the absorbance, $h\nu$ is the excitation energy in eV, and $r = 2$ is for indirect allowed transitions.

2.2.11. Surface Photovoltage Spectroscopy (SPS). SPS data was measured using a circular (2.5 mm diameter), semitransparent vibrating gold mesh disk (Kelvin Probe S, Besocke Delta Phi) controlled by using a Kelvin Control 7 oscillator/amplifier (Besocke Delta Phi) and mounted inside of a home-built vacuum chamber evacuated to 1.9×10^{-4} mbar. Samples were prepared by dropcoating an aqueous suspension of vanadate on fluorine-doped tin oxide (FTO), followed by annealing at 500 °C in air for 2 h, and were

https://doi.org/10.1021/acs.inorgchem.1c02511
Inorg. Chem. 2022, 61, 154–169

placed 1.0 mm underneath the Kelvin probe and connected electrically to the ground, as reported previously.[53] Illumination in the 0.8−4.13 eV regime was provided by light from a 150 W Xe lamp (PerkinElmer) and filtered through an Oriel Cornerstone 130 monochromator. The light exiting the monochromator had an FWHM (full width at half maximum) of 8−15 nm depending on the wavelength, and the intensity at the sample was 150 $\mu W/cm^2$ on average. The spectra were acquired by stepping the photon energy by 0.0124 eV every 5 s and by measuring the contact potential difference (CPD) value at each step. CPD values are reported relative to the CPD value in the dark. Positive values correspond to electrons moving toward the Kelvin probe and negative values correspond to electrons moving away from the Kelvin probe. To correct for drift effects, a baseline was established by measuring CPD values in the dark for at least 15 min before each scan and by fitting the CPD values to a linear graph, which was then subtracted from the raw data.

2.2.12. Photoelectrochemical (PEC) Measurements. A three-electrode setup was used in the PEC measurements. A Pt wire and Hg/Hg_2Cl_2 in 1.0 M KCl were used as the counter and reference electrodes, respectively, and a 0.1 M Na_2SO_4 aqueous solution with 20% methanol (pH 7) or 0.1 M K_2SO_4 (pH 7) served as the electrolyte. PEC measurements were performed after purging the electrolyte with N_2 for 10 min. Potentials were converted to a normal hydrogen electrode (NHE) after cell calibration with a $K_{3/4}Fe(CN)_6$ redox couple (E^0 = 0.358 V). For water oxidation, potentials were further converted to a reversible hydrogen electrode (RHE) according to the pH of the electrolyte. A 300 W Xe lamp served as the visible light source. The light intensity at the electrode was 100 $mW{\cdot}cm^{-2}$, as measured with a GaAsP photodetector connected to an ILT 1400 light meter from International Light Technologies. Electrodes of $Zn_4V_2O_9$ were fabricated by drop-casting 0.6 mL aqueous suspension (ca. 3 mg/mL) onto fluorine-doped tin oxide (FTO) glasses (0.385 cm^{-2}), followed by drying in air, and annealing at 500 °C in air for 2 h.

3. RESULTS AND DISCUSSION

3.1. Crystal Structure of Zinc Vanadates. $Zn_4V_2O_9$ is the most Zn-rich oxide in the ZnO-V_2O_5 pseudo-binary system and has structural similarities to zinc hydroxy vanadate hydrate $Zn_3(OH)_2V_2O_7{\cdot}2H_2O$ and another zinc-rich vanadate $Zn_3V_2O_8$. The latter two compounds are intermediates in the DES-involved precipitation synthesis of $Zn_4V_2O_9$; thus, the crystal structures of the aforementioned zinc vanadates are briefly described below to facilitate discussion on the reaction pathway toward $Zn_4V_2O_9$ and comparison of its properties to other zinc vanadates. The crystal structure of $Zn_3(OH)_2V_2O_7{\cdot}2H_2O$ has trigonal symmetry ($P\bar{3}m1$) and is composed of edge-sharing zinc oxide/hydroxide octahedra, $ZnO_4(OH)_2$, building a Brucite-type ($Mg(OH)_2$) layer stacked along the *c*-axis (Figure 1a).[54−56] Three of four octahedral sites in the close-packed layer of oxygen atoms are occupied by zinc atoms.[54−56] The remaining site is surrounded by vanadium tetrahedra, building a Kagome lattice with a hexagonal void space.[54−56] V−O−V pillars within the pyrovanadate ($[V_2O_7]^{4-}$) group keep the layers apart, creating a porous framework with an interlayer spacing of 7.231 Å. The large cavities are randomly filled by water molecules, which form hydrogen bonds with OH groups in the zinc oxide/hydroxide polyhedra.[54−56] $Zn_3V_2O_8$ crystallizes in the orthorhombic space group *Cmca*.[57] The edge-sharing $[ZnO_6]$ octahedron forms Kagome layers, made of corner-sharing triangles and hexagonal voids, along the *c*-axis (Figure 1b).[57] Unlike the flat Kagome lattice seen in $Zn_3(OH)_2V_2O_7{\cdot}2H_2O$, the layers in $Zn_3V_2O_8$ are buckled and thus provide a staircase geometry.[57] VO_4 tetrahedra allow the isolated layers to be stacked along the *b*-axis.[57] With the most zinc-rich composition, $Zn_4V_2O_9$ crystallizes in the monoclinic space group $P2_1$.[58] Out of eight crystallographically independent zinc atoms, five are 5-coordinated and the rest—Zn(3), Zn(6), and Zn(8)—are 4-coordinated (Figure 1c,d).[58] On the other hand, all four unique vanadium atoms are tetrahedrally coordinated.[58] The $[ZnO_5]^{8-}$ triangular bipyramids and $[Zn(3)O_4]$ tetrahedra share edges and corners to construct layers along the *c*-axis (Figure 1d, left).[58] Similar to the buckled Kagome layers in $Zn_3V_2O_8$, $Zn_4V_2O_9$ holds void spaces within its layer but with more variety: rectangular, hexagonal, and octagonal nets (Figure 1c, right).[58] The space between the layers is occupied by $[Zn(6)O_4]$ and $[Zn(8)O_4]$ tetrahedra as well as $[VO_4]$ tetrahedra (Figure 1d, right).[58]

3.2. Synthesis and Reaction Pathway. A deep eutectic solvent (DES) comprised of urea (hydrogen bond donor, m.p. 132−135 °C) and choline chloride (hydrogen bond acceptor, m.p. 302 °C) (Figure 2c) is employed for the synthesis of zinc-

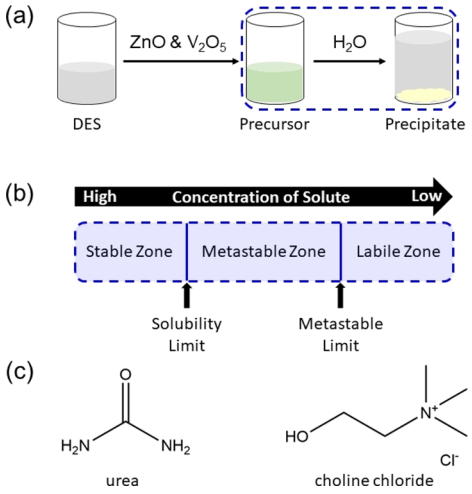

Figure 2. (a) Visual description of the synthesis route used in this study and (b) of a general precipitation process. (c) Molecular structures of urea and choline chloride, constituents of DES.

rich vanadates. With the eutectic composition (urea:choline chloride = 2:1), the mixture exhibits a significantly low melting point (~30 °C) due to a strong hydrogen bonding interaction between the components.[16−19] Importantly, stable binary transition metal oxides, such as ZnO and V_2O_5, are utilized as metal precursors in this study because of appreciable solubility in the choline chloride/urea DES, 1.31 M for ZnO at 70 °C and 0.030 M for V_2O_5 at 50 °C.[59] Preparation of the precursor solution involves the formation of metal-DES complexes—$[ZnClO{\cdot}urea]^-$ and $[VO_2Cl_2]^-$—upon dissolution,[59] providing a great atom economy in the metal oxide synthesis. When the binary metal precursors are fully dissolved in the eutectic mixture at 70 °C, a transparent solution is produced with color ranging from colorless to dark green depending on the amount of vanadium oxide dissolved. DI H_2O, a precipitation agent (often called antisolvent), is then introduced to the precursor solution to obtain white precipitates (Figure 2a). At the initial stage of antisolvent addition, the solution concentration gradually drops, and solutes eventually reach their solubility limit (Figure 2b). With the continuation of antisolvent addition, supersaturation is developed between the solubility curve and the metastable limit, at which nucleation proceeds spontaneously and rapidly.[60−64] Crystals then begin to grow if the supersaturation

https://doi.org/10.1021/acs.inorgchem.1c02511
Inorg. Chem. 2022, 61, 154−169

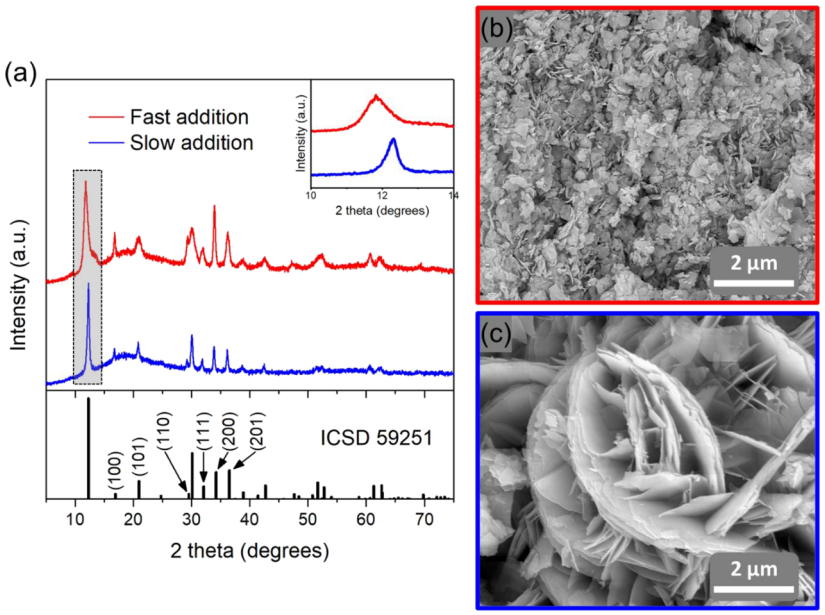

Figure 3. (a) PXRD patterns and (b, c) SEM images of the $Zn_3(OH)_2V_2O_7{\cdot}2H_2O$ precipitates from two different antisolvent addition rates (red, fast addition; blue, slow addition). ICSD 59251 indicates the $Zn_3(OH)_2V_2O_7{\cdot}2H_2O$ phase.

condition is maintained in the metastable zone with the desired precipitation condition (e.g., low temperature).[60−64]

To understand the precipitation process, three different experimental parameters—initial metal-to-metal ratio in the solution, temperature of the antisolvent, and antisolvent addition rate—were varied. Immediate addition of the antisolvent is employed with the temperature of the precursor and antisolvent being kept at 70 °C and room temperature, respectively, unless stated otherwise. Figure S1 shows powder X-ray diffraction patterns of precipitates obtained from the precursor solutions with various Zn/V ratios. All the powder samples contain $Zn_3(OH)_2V_2O_7{\cdot}2H_2O$ (ICSD 59251) as a main phase with a small unknown impurity appearing at ∼13° (marked with an asterisk). Phase identification based on such a weak and broad diffraction peak is limited. However, the position of the unknown peak matches well with that of the most intense diffraction peak of zinc carbonate hydroxide $Zn_5(OH)_6(CO_3)_2$ (ISCD 16583). The presence of a carbonate in the precipitate is further supported by the peak at 1622 cm^{-1} in the FTIR spectrum of the precipitate (Figure S2). The precipitate also shows a broad band at ∼3400 cm^{-1}, which is attributed to the O−H stretching vibration. Furthermore, crystalline zinc carbonate hydroxide was reported to precipitate from the solution of choline chloride/urea DES containing dissolved ZnO upon slow addition of water antisolvent.[30] The energy dispersive X-ray spectroscopy (EDS) mapping shows the homogeneous distribution of Zn, V, and O throughout all the powder samples (Figure S3). In addition, the average molar ratio of Zn:V from all samples is determined to be ∼2:1 from the quantitative X-ray analysis of multiple spots within the precipitate powders. Thus, we conclude that the zinc dihydroxide divanadate dihydrate together with an additional zinc-containing source, most likely zinc carbonate hydroxide, is precipitated independently of metal ratios in the precursor solution. Interestingly, we do not see any crystalline binary oxide phases such as ZnO, VO_2, V_2O_3, and V_2O_5, although the precipitation route using DES was reported to be a way to obtain binary metal oxides.[28−31] By adding water and/or ethanol antisolvent to the ZnO dissolved in the mixture of urea and choline chloride, Dong et al. prepared the zinc oxide nanoparticles with various morphology.[28−30] Similarly, Cu^{2+}-doped ZnO was obtained via the precipitation process by using copper nitrate as a dopant added in the antisolvent, consisting of an ethylene glycol and deionized water mixture.[31] We, for the first time, demonstrate that the ternary metal hydroxy oxide phase can be achieved by this route. The synthesis of $Zn_3(OH)_2V_2O_7{\cdot}2H_2O$ usually requires a heat treatment under hydrothermal or microwave conditions.[32,34,54−56,65−67] Accordingly, we believe that the precipitation process lowers the formation energy of the ternary zinc dihydroxide divanadate dihydrate phase.

Another parameter—the temperature of the antisolvent—was investigated for its impact on the formation of the crystalline phase and size/morphology of the precipitated particles. Precipitates obtained with antisolvent at different temperatures have almost identical powder X-ray diffraction patterns with $Zn_3(OH)_2V_2O_7{\cdot}2H_2O$ as a main phase (Figure S4). Various sizes of agglomerates made of 2D irregular-shaped nanosheets are observed from the precipitates. Notably, antisolvent at a low temperature yields bigger individual particles as compared to that obtained with a higher temperature of the antisolvent (Figure S4). This finding shares similarity with a report about controlling the size of Co nanoparticles based on the temperature of oleic acid in dichlorobenzene solution where a $Co_2(CO)_8$ precursor was injected into.[68] When a lower temperature precursor solution was injected, larger cobalt particles with broad size distributions formed.[68] A quick addition method is also one of the crucial parameters in obtaining nanosized particles. Therefore, a fast injection method with varying temperatures of the antisolvent controls the particle size within the nanoregime.

We investigated the addition rate of the antisolvent as the third parameter for the precipitation process. The main diffraction peaks of precipitates obtained from both slow and fast addition methods are indexed to $Zn_3(OH)_2V_2O_7{\cdot}2H_2O$

https://doi.org/10.1021/acs.inorgchem.1c02511
Inorg. Chem. 2022, 61, 154−169

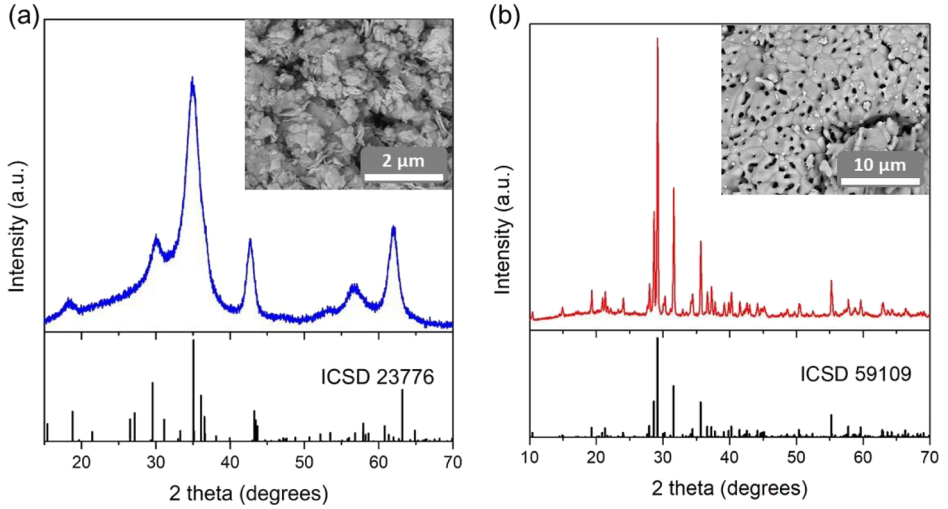

Figure 4. PXRD patterns and SEM images of (a) $ZnO/Zn_3V_2O_8$ and (b) $Zn_4V_2O_9$ obtained by heating the precipitate at 400 and 837 °C, respectively. ICSD 23776 and 59109 indicate the $Zn_3V_2O_8$ and $Zn_4V_2O_9$ phases, respectively.

(Figure 3). The SEM image of the fast addition method shows irregular-shaped aggregates made of nanosheets with a thickness of a few nanometers. In contrast, the slow addition method produces bouquet-shaped agglomerates. The sheet-like individual particles have a similar thickness as those from the fast addition method. However, the exfoliated individual particles form micrometer-sized three-dimensional flower-like morphology. When the room temperature solvent is added fast to the precursor solution, the reaction mixture rapidly reaches the labile zone beyond the metastable limit. Thus, the immediate precipitation occurs with a fast nucleation rate, which is responsible for the resulting small particles. On the other hand, the slow addition method allows the supersaturation (from low to high concentration level) to be maintained in the metastable zone for extended hours. The dropwise addition helps the reaction mixture remain at the warm temperature (70 °C). As a result, a significantly slower nucleation rate is achieved followed by particles' growth with time. The different morphology/sizes of particles observed by SEM are validated by the PXRD results (Figure 3a). First, the shift of the most intense diffraction peak to the lower diffraction angles is observed from the fast addition method. Considering that water molecules randomly occupy the channels,[54−56] the difference in the diffraction peak position could indicate that the amount of adsorbed H_2O molecules can vary depending on the antisolvent addition rate—the fast addition rate results in expansion of the interlayer spacing by ∼4.1% as compared to the slow addition method (inset to Figure 3a). Thus, the chemical formula of zinc hydroxy vanadate hydrate should be modified to $Zn_3(OH)_2V_2O_7{\cdot}nH_2O$ ($n \geq 0$). We can understand the variation in interlayer distance based on the structural similarity between β-alumina and $Zn_3(OH)_2V_2O_7{\cdot}nH_2O$. The β-alumina $(M_2O)_x{\cdot}11Al_2O_3$ (M = monovalent cation, $1.2 < x < 1.3$) has a layered structure with spinel blocks made of $[AlO_4]$ tetrahedra and $[AlO_6]$ octahedra.[69−71] Reminiscent of the V−O−V pillar in $Zn_3(OH)_2V_2O_7{\cdot}nH_2O$, Al−O−Al bonds separate the spinel blocks of the β-alumina, creating a rigid framework.[69−71] Various monovalent cations can occupy the interlayer spacing within the channel.[69−71] Likewise, the open framework within zinc dihydroxide divanadate can host different molecular species other than water molecules. The observed expansion of interlayer distance thus could be due to the presence of additional molecular species from the choline chloride:urea mixture trapped in the channel. We also noticed that the relative intensity of diffraction peaks varies depending on the antisolvent addition rate. Unlike the slow addition method, the PXRD pattern of the fast addition method shows significantly enhanced peak intensities for (100), (200), and (110) planes. We can deduce that the nanosheets are oriented along the [100] and [110] directions corresponding to the extended layers of zinc oxide/hydroxide octahedra and the face diagonal of the trigonal unit cell, respectively. Therefore, we conclude that the nanosheets are grown anisotropically, resulting in the preferred orientation. In addition, we noticed that {h00} diffraction peaks of the two PXRD patterns have a similar full width at half maximum (FWHM), indicating that the thicknesses of individual sheets are alike: ∼29.8 nm calculated by the Scherrer equation. However, other peaks corresponding to (101), (111), and (201) planes have noticeably broadened peak widths for the fast addition method as compared to that of the slow addition method. Based on the anisotropic crystal growth along the [100] together with a diffraction peak broadening stemming from a decrease in crystalline domain size, our finding suggests that the two-dimensional nanosheets of smaller size are produced by the fast addition method.

According to the previous reports, preparation of $Zn_3V_2O_8$ is readily available by heat treatment of $Zn_3(OH)_2V_2O_7{\cdot}2H_2O$ between 200 and 500 °C where dehydration occurs.[34,65] The PXRD data of the sample after heating the precipitate at 400 °C in air (Figure 4a) agrees with the literature data as the diffraction peaks correspond to $Zn_3V_2O_8$ (ICSD 23776), albeit the phase has low crystallinity. A change in dwelling time does not have an impact on the crystalline phase observed. However, the pronounced shift of peaks at ∼43° and 62° 2θ to a lower diffraction angle is observed, likely due to an expanded unit cell. Interestingly, the SEM image of $Zn_3V_2O_8$ shows that the size and morphology of the nanosheets remain unaltered before and after the heat treatment. Upon heating the precipitate at 400 ° C, an intensity of the band in the FTIR spectrum corresponding to O−H vibrations is reduced, while the peak at 1620 cm^{-1} corresponding to carbonate is eliminated (Figure S2). This further proves that CO_2 and H_2O are evolved upon heating of the precipitate consisting of

https://doi.org/10.1021/acs.inorgchem.1c02511
Inorg. Chem. 2022, 61, 154−169

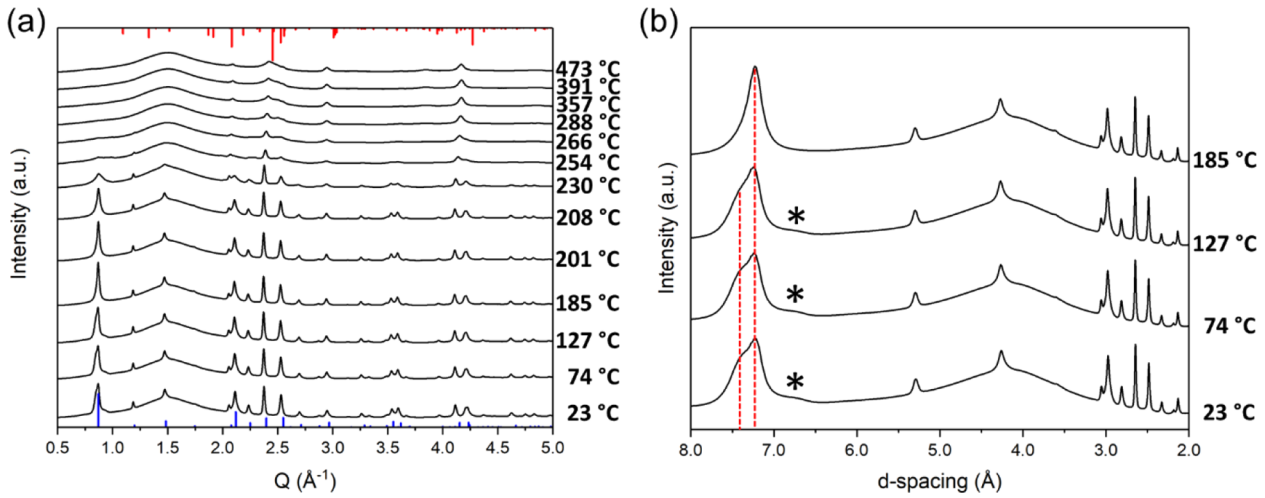

Figure 5. (a) Selected high-temperature powder diffraction patterns upon heating up to 473 °C with calculated patterns shown for $Zn_3(OH)_2V_2O_7 \cdot 2H_2O$ (blue bars, bottom) and $Zn_3V_2O_8$ (red bars, top). (b) Two overlapping diffraction peaks corresponding to the two different interlayer distances within $Zn_3(OH)_2V_2O_7 \cdot 2H_2O$ are highlighted by red dotted lines. A peak tentatively assigned to $Zn_5(OH)_6(CO_3)_2$ is marked with an asterisk.

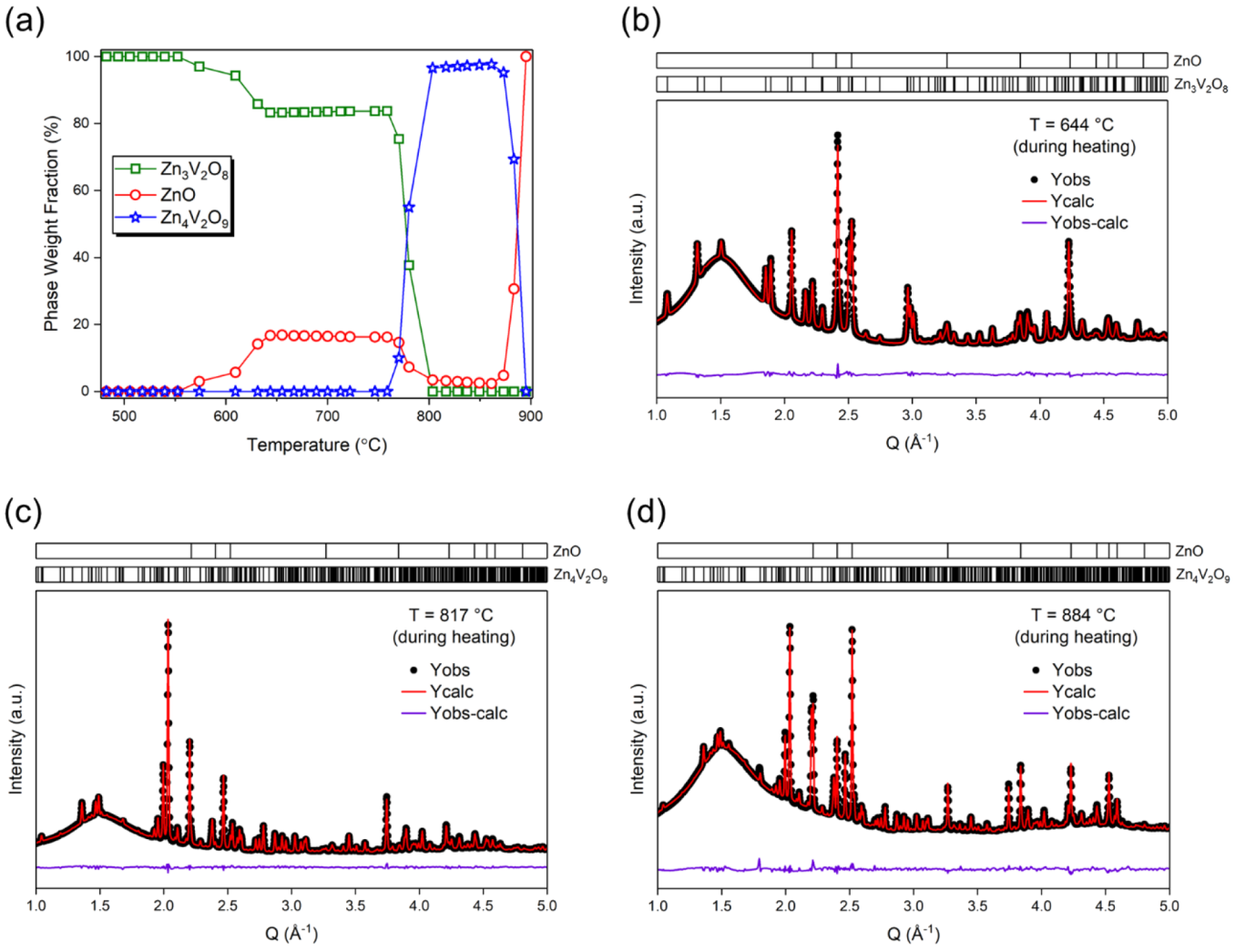

Figure 6. (a) Summary of HT-PXRD data from sequential Rietveld refinements for the precipitate. (b–d) Refinement results of selected diffraction patterns collected at different temperatures during heating. The side product Zn_2SiO_4 is omitted for clarity. See Table S1.

zinc carbonate hydroxide and $Zn_3(OH)_2V_2O_7 \cdot 2H_2O$ to yield a $ZnO/Zn_3V_2O_8$ intermediate. Based on the homogeneous distribution of Zn and V from the elemental EDS maps (Figure S5) together with the absence of the crystalline

https://doi.org/10.1021/acs.inorgchem.1c02511
Inorg. Chem. 2022, 61, 154–169

diffraction peak of secondary phases, we hypothesize that amorphous ZnO is deposited on the host material $Zn_3V_2O_8$ from the heating of the precipitate.

With further heating of the precipitate, we obtained another zinc-rich vanadate. The powder X-ray diffraction peaks of the sample after annealing of the precipitate at 837 °C are indexed to $Zn_4V_2O_9$ (ICSD 59109) as shown in Figure 4b. It should be noted that the purity of the powder sample varies depending on the Zn/V ratio in the precursor solution (Figure S6). The synthetic condition with the 1:1 ratio of Zn/V yields a phase-pure sample, whereas contamination with ZnO is observed when the zinc-rich or vanadium-rich compositions are loaded as the precursor. Taking into account the fact that the target compound $Zn_4V_2O_9$ does not decompose at temperatures below 837 °C, as discussed further, we believe that the presence of ZnO impurity is due to the excess zinc source $Zn_5(OH)_6(CO_3)_2$ that precipitated upon the antisolvent addition. The SEM image of $Zn_4V_2O_9$ shows agglomerates sized up to ~27 μm with porous morphology. Densification and sintering are the most common phenomena of solid-state materials resulting from heat treatments. However, it has been reported that thermal decomposition of metal hydroxides such as $Ni(OH)_2$ and $Mg(OH)_2$ can lead to the formation of porous metal oxides NiO and MgO.[72−74] Therefore, the thermal dehydration of $Zn_3(OH)_2V_2O_7{\cdot}2H_2O$ is responsible for the porosity formation as shown in Figure 4b.

We further investigated the reaction pathway toward zinc-rich vanadates using *in situ* high-temperature powder X-ray diffraction (HT-PXRD). Figure 5 shows phase evolution PXRD patterns upon heating of the precipitate from room temperature to 473 °C. The starting material is composed of $Zn_3(OH)_2V_2O_7{\cdot}2H_2O$ as a major phase and tentatively $Zn_5(OH)_6(CO_3)_2$ (marked with an asterisk) as a minor phase. Notably, two overlapping peaks are observed at ~0.7 $Å^{-1}$, indicating two different interlayer distances within $Zn_3(OH)_2V_2O_7{\cdot}2H_2O$ (7.231 and 7.387 Å). Upon heating up to 185 °C, the diffraction peak at the lower Q value is gradually disappearing. According to the previous reports,[54−56] the adsorbed water can be thermally removed at 200 °C, so more than 50% of the volume between the layers is being unoccupied. The dehydrated product still preserves the layered structure with a contraction in the interlayer distance by less than 0.1 Å, indicating that water is not critical to the structure.[56] Therefore, our experimental results suggest that the deintercalation of water and an additional molecular species from the channel occurs at different rates upon heating, while the layered structure is preserved. In turn, the intensity of the diffraction peak at a higher Q value corresponding to the interlayer distance of 7.231 Å begins to decrease above 200 °C when the layered structure supported by V−O−V pillars collapses. The $Zn_3(OH)_2V_2O_7{\cdot}2H_2O$ phase finally disappears and the broad diffraction peaks of $Zn_3V_2O_8$ become dominant above 230 °C, validating the formation of the oxide nanoparticles as evidenced from the *ex situ* experimental data (Figure 4a).

The narrowing of diffraction peaks for $Zn_3V_2O_8$ and ZnO is observed starting from 482 °C and 563 °C, respectively, suggesting the growth of crystals from the nanoscale to micrometer scale. Upon further heating up to 747 °C, there is no change in the observed diffraction patterns except for a diffraction peak shift stemming from thermal expansion. It should be noted that $Zn_4V_2O_9$ starts to appear above 759 °C, and a significant increase in its phase fraction is observed until 804 °C (Figure 6 and Table S1). On the other hand, fractions of $Zn_3V_2O_8$ and ZnO gradually decrease within this temperature range, revealing that $Zn_4V_2O_9$ is a product of the reaction between $Zn_3V_2O_8$ and ZnO intermediates. $Zn_4V_2O_9$ is thermally stable until 861 °C, above which the ZnO phase fraction starts to increase due to decomposition of $Zn_4V_2O_9$. Another decomposition product, $Zn_3V_2O_8$, is not seen in the diffraction pattern because it is unstable above 800 °C.[75] We also noticed that a side product, Zn_2SiO_4, appears from 884 °C and stays until the end of the experiment due to the side reaction with the silica capillary material. Upon cooling from 900 °C, none of the ternary zinc vanadate phases are observed until 840 °C, below which $Zn_3V_2O_8$ starts to appear. However, $Zn_3V_2O_8$ is only stable until 548 °C, which could be due to the fast cooling rate (20 °C/min) employed. Diffraction peaks of another ternary zinc vanadate β-$Zn_2V_2O_7$ show up below 823 °C and stay until the end of cooling. Importantly, the most zinc-rich phase $Zn_4V_2O_9$ is not recovered after its complete decomposition, although $Zn_3V_2O_8$ and ZnO coexist in the powder sample upon cooling from 823 °C to 548 °C.

Differential scanning calorimetry (DSC) and thermogravimetric analysis (TGA) of the precipitate support findings from HT-PXRD and provide more accurate determination for phase transformation temperatures (Figure 7). The first broad

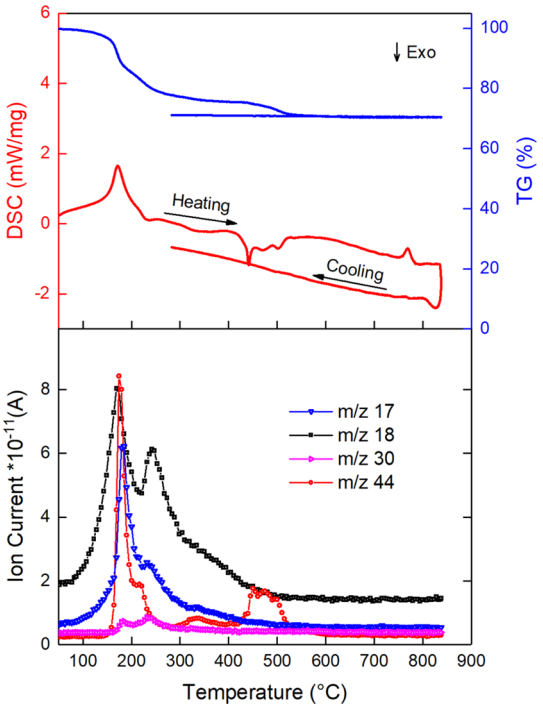

Figure 7. DSC/TGA upon heating and cooling of the precipitate (top). Released gas data collected using the mass spectrometer upon heating (bottom).

endothermic peak centered at 171 °C is observed along with the sample mass loss of ~9%. The signals of m/z 17 and 18 from the mass spectrometer show the highest ion current at 184 and 169 °C, respectively, suggesting that the dehydration process from $Zn_3(OH)_2V_2O_7{\cdot}2H_2O$ contributes to the first thermal event. According to Shi et al., the water removal can occur from the temperature as low as 40 °C.[65] Therefore, our hypothesis is further supported by the gradual decrease in sample mass from 76 °C, which coincides with the gradual

https://doi.org/10.1021/acs.inorgchem.1c02511
Inorg. Chem. 2022, 61, 154−169

increase in m/z 17 and 18 intensity. Interestingly, another gas signal of m/z 44 begins to increase drastically from 153 °C and reaches its highest value at 174 °C. Since $Zn_3(OH)_2V_2O_7\cdot 2H_2O$ holds a porous framework, the gas signal is likely from a fragment ion, such as CH_3CHNH_2 of additional molecular species trapped in the channel. Similarly, the signal m/z 30 can be understood by another fragmentation such as CH_2NH_2. The first broad exothermic peak at 232 °C is then attributed to the formation of $Zn_3V_2O_8$ as seen in a previous report.[65] It should be noted that the ion currents of m/z 17 and 18 increase again from 221 °C and reach the local maximum at 237 °C. Sinhamahapatra et al. showed that $Zn_5(CO_3)_2(OH)_6$ undergoes thermal decomposition in two steps: dehydration at 250−325 °C to yield $Zn_5(CO_3)_2O_3$, followed by carbonate removal at 325−440 °C, leaving ZnO as a final product.[76] We thus hypothesized that the second increase in the intensities of signals m/z 17 and 18 is due to the water removal from $Zn_5(CO_3)_2(OH)_6$. The m/z 44 signal from 288 to 524 °C, which can be assigned to removing carbonate from $Zn_5(CO_3)_2(OH)_6$, further supports our hypothesis. In turn, a group of exothermic peaks appears between 417 and 527 °C. Although individual assignments of them are limited due to the peak overlap, we can deduce from HT-PXRD data that the growth of $Zn_3V_2O_8$ and ZnO crystallization contribute to the exothermic thermal events. Finally, the endothermic peak with the onset temperature of 754 °C is assigned to the formation of $Zn_4V_2O_9$ from the reaction between $Zn_3V_2O_8$ and ZnO. There is no measurable DSC signal or sample mass loss observed afterward. Based on the HT-PXRD and DSC/TGA data, the suggested reaction pathway toward $Zn_4V_2O_9$ formation is as follows:

$$5Zn_3(OH)_2V_2O_7\cdot 2H_2O + Zn_5(CO_3)_2(OH)_6 \xrightarrow{>232^\circ C} 5Zn_3V_2O_8 + 5ZnO + 18H_2O(g) + 2CO_2(g) \xrightarrow{754^\circ C} 5Zn_4V_2O_9 \quad (1)$$

Obtaining the zinc-rich vanadate $Zn_4V_2O_9$ has been a great challenge and required a tedious reaction procedure. Waburg and Müller-Buschbaum used a CO_2-laser generated flux and ZnO/V_2O_5 mixture for the synthesis.[58] Even with a pelletized mixture of ZnO and V_2O_5, an extended period (60−72 h) of sintering at 800−850 °C in air was required.[77] In addition, the reaction product had to be quenched in liquid nitrogen due to the metastable characteristic of $Zn_4V_2O_9$.[77] According to another report, heating of the premade ternary oxide $Zn_3V_2O_8$ mixed with ZnO at 835 °C, followed by rapid quenching, resulted in the formation of the target compound.[78] However, a long reaction time (20 h) at the elevated temperature was still a crucial step during the heat treatment.[78] In contrast, our synthetic method provides a complete reaction within 30 s of annealing of the precipitate at 837 °C and yields phase-pure $Zn_4V_2O_9$. Such a fast reaction could stem from the labile precursor nanoparticles $Zn_3(OH)_2V_2O_7\cdot 2H_2O$ and $Zn_5(CO_3)_2(OH)_6$ being well mixed as supported by the elemental mapping. More specifically, the intermediate oxides $Zn_3V_2O_8$ and ZnO derived from the precursors still maintain the intimate mixing, resulting in lowering of a diffusion barrier between the solids. It could also be possible that the intermediate oxides $Zn_3V_2O_8$ and ZnO formed during the ramping stage of heating could have enhanced reactivity as compared to the premade counterparts. Therefore, we believe that a suitable choice of precursors can potentially open a venue toward preparation of metastable materials. When it comes to cooling, we confirm that quenching of the reaction mixture is not necessary as there is no difference in the PXRD patterns obtained from quenching and slow natural-cooling methods (Figure S7).

We further investigated the metastability of $Zn_4V_2O_9$ using the *in situ* experiment. Figure S8 shows selected powder diffraction patterns of synthesized $Zn_4V_2O_9$ upon heating followed by cooling. Partial decomposition of the zinc-rich oxide is observed above 880 °C as evidenced from the appearance of diffraction peaks corresponding to ZnO, consistent with the HT-PXRD data of the precipitate. It should be noted that cooling of the reaction mixture prior to complete decomposition of $Zn_4V_2O_9$ leads to its phase recovery, unlike the *in situ* experimental result of precipitate discussed earlier. Moreover, unknown diffraction peaks (marked with a transparent green box in Figure S8) appear at 520 °C and further grow until 400 °C. We conclude that the partial decomposition of $Zn_4V_2O_9$ occurs upon heating to 900 °C and further cooling at a moderate rate (10 °C/min). *Ex situ* experimental data shown in Figure S9 additionally demonstrates the metastable character of $Zn_4V_2O_9$—its partial decomposition as a result of reheating at a particular temperature (650 °C) for 6 h.

The DES precipitation synthesis of $Zn_4V_2O_9$ described above is fundamentally different from the combustion synthesis route from DES previously used to synthesize $Zn_2V_2O_7$ and ZnV_2O_6.[23,24] The principal difference is that in the combustion synthesis, the ratio of the metals in the DES controls the stoichiometry of the ternary oxide formed at elevated temperatures, while DES is removed via combustion. On the contrary, in the DES precipitation synthesis, the composition of the precipitate is dictated by the solubility of the metal-containing solutes in the antisolvent. Therefore, the ratio of metals in the resulting ternary oxide obtained by a rapid heating of the precipitate may significantly differ from the metals' ratio in the DES. Additionally, it is needless to remove the DES via combustion since the precipitate is typically a mixture of hydroxides and carbonates, which transform into oxides upon gentle heating.

3.3. Raman Spectroscopy. Raman spectroscopy is utilized to investigate vibrational properties of solid products. Figure 8 shows that the Raman spectrum of the precipitate agrees well with that of $Zn_3(OH)_2V_2O_7\cdot 2H_2O$ reported in the literature[79] without any detectable peaks from binary metal oxides (ZnO and V_2O_5, see Figure S10). All the peaks can be understood by vibrations of $[V_2O_7]^{4-}$ units (Table S2).[80] The highest intensity from the band at 863 cm^{-1} is assigned to the symmetric stretching mode of $[VO_3]$.[80] The combination of asymmetric stretching mode from $[VO_3]$ and [V−O−V] is confirmed by the peak at 795 cm^{-1}.[80] The Raman bands at 475 and 427 cm^{-1} are attributed to asymmetric $[VO_3]$ bending modes, while a symmetric bending mode of $[VO_3]$ is ascribed to the peak at 325 cm^{-1}.[80] Furthermore, the [V−O−V] bending mode contributes to the Raman peak at 249 cm^{-1}.[80] A weak broad band observed at ∼927 cm^{-1} could arise from the strongest Raman peak of $Zn_5(CO_3)_2(OH)_6$ being shifted from 1062 cm^{-1} due to its semicrystalline nature.[81−83] The Raman spectrum of the intermediate phase $ZnO/Zn_3V_2O_8$ only shows a broad peak at 786−873 cm^{-1} (Figure S10), which might be from the semicrystalline form of $Zn_3V_2O_8$.[82−84] The loss of long-range translational symmetry causes all phonons in the

https://doi.org/10.1021/acs.inorgchem.1c02511
Inorg. Chem. 2022, 61, 154−169

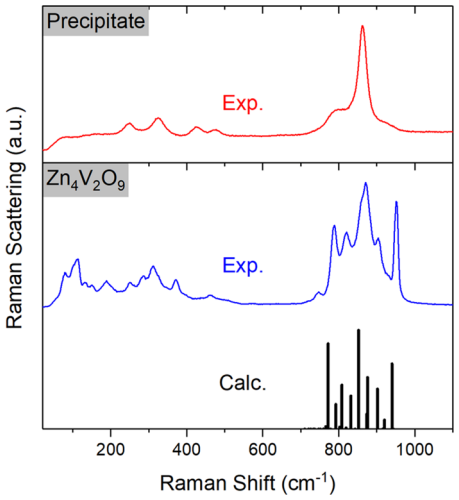

Figure 8. Experimental Raman spectra of the precipitate (top) and $Zn_4V_2O_9$ (bottom). The calculated Raman active modes are shown in black bars.

Brillouin zone to become Raman-active, resulting in band broadening.[82,83]

The Raman spectrum of the synthesized $Zn_4V_2O_9$ is shown in Figure 8. With vanadium metal being exclusively in a tetrahedral geometry, the observed Raman bands are assigned to vibrational modes based on the free vanadate unit $[VO_4]^{3-}$.[85] Although the reduced symmetry of the vanadate tetrahedra in $Zn_4V_2O_9$ removes degenerate vibrational modes, all other modes are still Raman-active.[85] The origin of peaks in the high-wavenumber region (800−1000 cm^{-1}) was reported to be the symmetric stretching mode of $[VO_4]^{3-}$.[85] However, individual peak assignments in this region were not available until now. With DFT-calculated Raman-active vibrational modes, we found out that each Raman peak is mainly contributed by a stretching mode of a discrete V−O bond stemming from a particular vanadium coordination polyhedron (exception: 874, 792, and 766 cm^{-1} as shown in Table 1). We thus conclude that the presence of four nonequivalent vanadium sites within the unit cell is responsible for the splitting of the internal $[VO_4]^{3-}$ modes. The Raman peaks at 462 and 370 cm^{-1} are assigned to asymmetric bending modes, whereas the band at 285 cm^{-1} is contributed by the symmetric bending mode.[85] Moreover, peaks corresponding to the lattice vibrational modes appear at the low-wavenumber region (80−250 cm^{-1}).[85]

3.4. X-ray Photoelectron Spectroscopy. To investigate the elemental composition and chemical state of metals and oxygen on the surface of $Zn_4V_2O_9$ and V_2O_5 (reference sample), X-ray photoelectron spectroscopy (XPS) is carried out. The Zn 2p peaks together with a Zn-modified Auger parameter (2010.73 eV) from $Zn_4V_2O_9$ agree well with those of ZnO,[86] confirming that a divalent zinc cation is bonded to oxide anions (Figure S11). Figure 9 shows the O 1s and V 2p core-level spectra in the binding energy range from 513 to 537 eV. The O 1s peak is recognized as a combination of two different species appearing at ∼530.17 and ∼ 531.87 eV. The narrow peak at the low binding energy is ascribed to the lattice oxygen, whereas the broad one at the high binding energy is due to the presence of oxygen defects/surface-adsorbed oxygen.[87] The spin−orbit splitting of V $2p_{3/2}$ and V $2p_{1/2}$ is observed in both samples. Considering peak positions and the

Table 1. Experimental and Calculated Raman Data of $Zn_4V_2O_9$[a]

	Raman shift (cm^{-1})			
peak	experiment	calculation	calculated Raman activity (arb. units)	assignment
1	952	940	1991	$\nu(V_3\text{-}O_{11})$
		921	335	$\nu(V_2\text{-}O_{17})$
2	903	902	1248	$\nu(V_4\text{-}O_{16})$
3	870	876	1590	$\nu(V_2\text{-}O_{17})$
		874	523	$\nu(V_1\text{-}O_{13}) + \nu(V_2\text{-}O_2)$
		852	2981	$\nu(V_1\text{-}O_{13})$
4	819	832	1045	$\nu(V_1\text{-}O_1)$
		819	103	$\nu(V_4\text{-}O_{14})$
		808	1366	$\nu_s(O_4\text{-}V_3\text{-}O_8)$
5	788	792	797	$\nu_s(O_4\text{-}V_3\text{-}O_8) + \nu(V_2\text{-}O_{15})$
		772	2583	$\nu(V_4\text{-}O_{12})$
6	748	766	144	$\nu(V_2\text{-}O_2) + \nu(V_1\text{-}O_{14})$
7−8	462, 370			$\delta_{as}(VO_4)^{3-}$
9	285			$\delta_s(VO_4)^{3-}$
10−15	250, 188, 151, 132, 112, 80			lattice vibrations

[a] ν: bond-stretching vibration; δ: angle-bending vibration; s: symmetric; as: asymmetric. The assignments for peaks 7−15 are based on a previous report.[85]

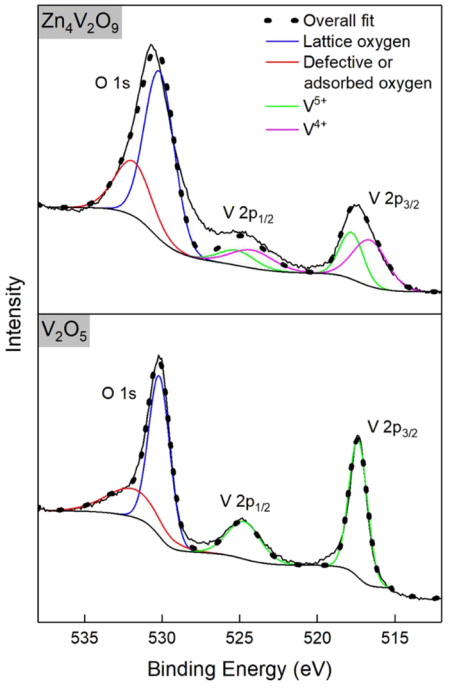

Figure 9. XPS data of the O 1s and V 2p regions from $Zn_4V_2O_9$ (top) and a reference V_2O_5 (bottom).

Coster−Kronig effect,[86,88] the symmetric peaks at ∼517.37 eV with an FWHM (full width at half maximum) of 1.38 eV (V $2p_{3/2}$) and at ∼524.74 eV (FWHM = 2.50 eV, V $2p_{1/2}$) from the reference V_2O_5 indicate that vanadium is in the pentavalent state. On the other hand, $Zn_4V_2O_9$ shows a significant peak broadening: FWHMs of 2.66 and 5.82 eV for V $2p_{3/2}$ and V $2p_{1/2}$, respectively. Such a wide peak suggests that a multiplet structure of vanadium cation is available due to unpaired

https://doi.org/10.1021/acs.inorgchem.1c02511
Inorg. Chem. 2022, 61, 154−169

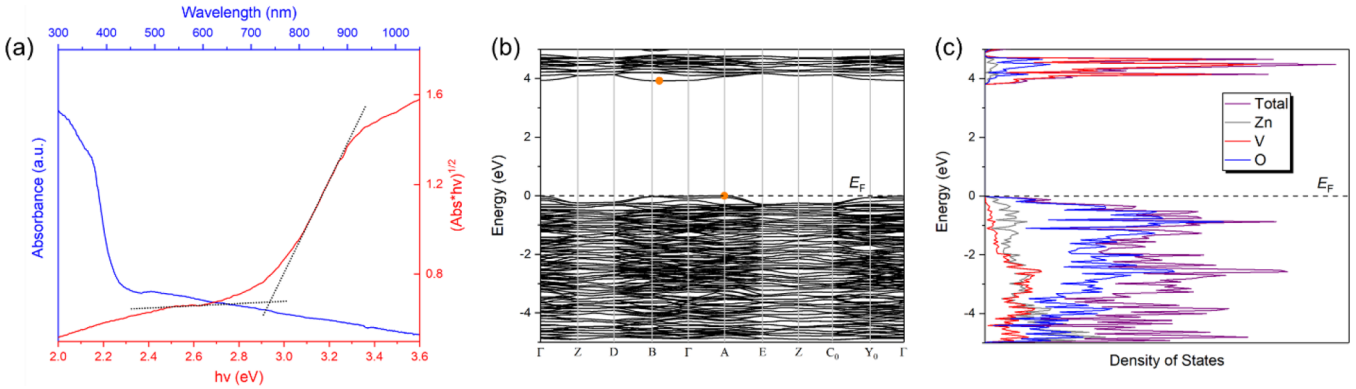

Figure 10. (a) UV−vis spectrum plotted with a corresponding Tauc plot of $Zn_4V_2O_9$. (b) Band structure and (c) projected total density of states calculated for $Zn_4V_2O_9$.

electrons.[86] Based on the peak position (517.26 eV for V $2p_{3/2}$), however, we can deduce that V^{5+} also exists. A reasonable deconvolution of the V 2p peaks is achieved with two pairs of spin−orbit doublets, peaks at 517.8 eV (FWHM = 1.78 eV) and 525.2 eV (FWHM = 2.70 eV) corresponding to V $2p_{3/2}$ and V $2p_{1/2}$ of V^{5+}, while the other two peaks at 516.6 eV (FWHM = 2.59 eV) and 524.2 eV (FWHM = 3.25 eV) indicate the reduced oxidation state of vanadium, V^{4+}. The % concentrations of V^{4+} and V^{5+} are 59 and 41%, respectively. Therefore, we conclude that the precipitation with antisolvent followed by the annealing process led to the mixed-valent vanadium species present in $Zn_4V_2O_9$.

3.5. Electronic Structure and Band Gap. The optical property of $Zn_4V_2O_9$ is evaluated by using diffuse reflectance UV−vis spectroscopy at room temperature (Figure 10a). The absorption edge is observed at ∼428 nm with the indirect band gap of 2.94 eV determined from a Tauc plot. In addition, a broad optical absorption is observed in the range of 2.25−2.94 eV, suggesting that excitation of defect states is available in the sub-band gap region.[89] From the XPS analysis, we confirmed that the missing oxide anions create reduced vanadium species (V^{4+}) in $Zn_4V_2O_9$ prepared by the precipitation method. Furthermore, V^{4+} in the oxygen vacancy-containing ZnV_2O_6 and $Zn_2V_2O_7$ gave rise to the additional states in between the valence and conduction bands according to the previous reports.[23,24] Consequently, we conclude that the absorption tail originates from the V^{4+} mid-gap states.

We calculated the electronic structure of $Zn_4V_2O_9$ using the HSE06 hybrid functional (Figure 10b,c). Based on the band structure, a band gap of 3.93 eV is obtained. The ∼1.0 eV difference in the calculated and experimental band gaps is surprising given the accuracy of HSE06 with insulating systems. Nevertheless, the band structure calculation also reveals an indirect band gap, which is consistent with experiment. The conduction band is primarily composed of empty V 3d states with a minor contribution of empty Zn 4s states. On the other hand, the O 2p states are dominant in the valence band with some contribution from the completely filled Zn 3d orbitals.

3.6. Photoluminescence. According to the combinatorial library made by Mordkovich et al., the intensity of yellow luminescence (560 nm) varied depending on the vanadium concentration in the ZnO-V_2O_5 system.[40] The samples in the concentration range of 32−40% V exhibited a high luminescence efficiency with the maximum value obtained at 33% V.[40] When the luminescence dependency on chemical composition was compared with the phase diagram of the ZnO-V_2O_5 system, the yellow emission reached the maximum intensity in the area where $Zn_4V_2O_9$ (33% V) and $Zn_3V_2O_8$ (40% V) coexisted.[40] Although the finding was based on the low-crystallinity samples, later reports further proved that $Zn_3V_2O_8$ possesses a promising yellow luminescence property with the quantum yield ranging between 43 and 52%.[36,37,39] Inspired by the previous work, we performed photoluminescence (PL) measurement for the as-synthesized $Zn_4V_2O_9$ with excitation wavelengths of 310 and 320 nm. Despite the incident photon energy being sufficient to excite the oxide phase, there was no discernable emission observed. Indeed, exciting $Zn_4V_2O_9$ at 310 and 320 nm at 77 K also did not produce any observable luminescence. In general, the origin of zinc vanadate phosphors' luminescence is the one-electron charge transfer (CT) from the O 2p orbital to the vacant 3d orbital of V^{5+} in VO_4 tetrahedra with T_d symmetry.[37] The significantly different luminescence quantum efficiencies—0.09 and 52% for $Zn_2V_2O_7$ and $Zn_3V_2O_8$, respectively—were attributed to the different metal interactions stemming from their crystal structures.[37] Unlike the dimerized VO_4 of $Zn_2V_2O_7$, the isolated vanadium oxide tetrahedra in $Zn_3V_2O_8$ are responsible for a strong interaction between the adjacent V cations and weak interaction between Zn and V cations, providing the enhancement in the exciton diffusion lifetime.[37] Importantly, $Zn_4V_2O_9$ also consists of isolated VO_4 tetrahedra, leading us to predict a strong yellow emission. However, the reduced vanadium species (V^{4+}) created by oxygen vacancies, as shown in the XPS data, possibly diminish the CT transition.

3.7. Surface Photovoltage Spectroscopy and Photoelectrochemical Experiments. Next, we employ surface photovoltage spectroscopy (SPS) to characterize the ability of $Zn_4V_2O_9$ to generate and separate charge carriers under illumination. In SPS, a vibrating Kelvin probe measures the contact potential difference (CPD) of a material.[90−92] The CPD change under illumination corresponds to a surface photovoltage. The data for the $Zn_4V_2O_9$ particle film on an FTO substrate is shown in Figure 11. The negative photovoltage is attributed to the injection of photogenerated electrons in $Zn_4V_2O_9$ into the FTO substrate, as shown in the inset. On this basis, the material is n-type. Using the tangent line for the major photovoltage feature, the compound has a 2.95 eV band gap, similar to the optical band gap of the material. However, the weak photovoltage signal at 2.25−2.95 eV suggests the presence of sub-band gap states. These states likely correspond to the V^{4+} ions that are also responsible for

https://doi.org/10.1021/acs.inorgchem.1c02511
Inorg. Chem. 2022, 61, 154−169

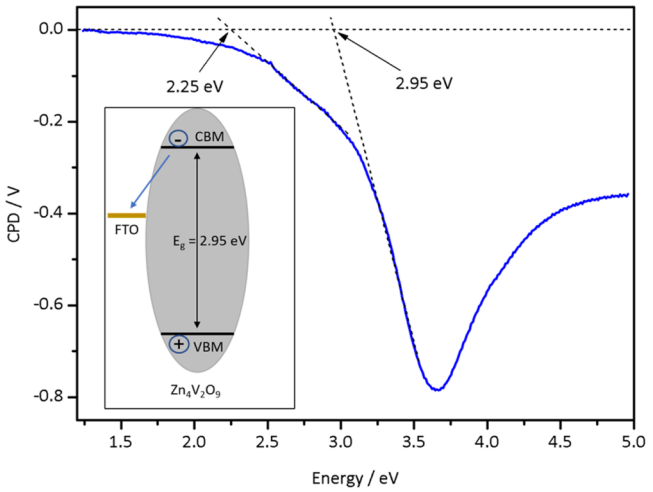

Figure 11. Surface photovoltage data of a $Zn_4V_2O_9$ particle film on FTO. Inset: charge transfer causing the photovoltage signal.

the visible absorption tail in the optical spectra. The sub-band gap signal is much more pronounced than for ZnV_2O_6[24] or $Zn_2V_2O_7$,[23] which indicates that $Zn_4V_2O_9$ has a higher V^{4+} concentration. This is consistent with the XPS data.

To determine if $Zn_4V_2O_9$ is able to facilitate photoelectrochemical reactions, linear sweep voltammograms (Figure 12) under chopped simulated sunlight (from a 300 W Xe arc lamp) were obtained on $Zn_4V_2O_9$-coated FTO electrodes (Figure S12) in degassed aqueous 0.1 M Na_2SO_4 with 20% (v:v) added methanol or in aqueous 0.1 M K_2SO_4. Weak photocurrents were observed when the applied potentials exceeded +0.15 V vs NHE in aqueous methanol and +0.6 V vs NHE in aqueous 0.1 M K_2SO_4. In the latter electrolyte, the current is attributed to water oxidation, although no O_2 could be detected at this low activity. Based on the photo-onset potential in aqueous methanol, the Fermi level in $Zn_4V_2O_9$ is at +0.15 V vs NHE (0.56 V RHE). Overall, $Zn_4V_2O_9$ is 10 times less photoactive than the ZnV_2O_6 phase for which methanol oxidation photocurrents of 20 $\mu A \cdot cm^{-2}$ at 1.6 V vs RHE were measured under 150 $mW \cdot cm^{-2}$ visible light illumination.[24] The lower activity of $Zn_4V_2O_9$ is attributed to the high concentration of V^{4+} sub-band gap states, which promotes recombination with the photogenerated holes. A similar role of reduced Ti^{3+} sites had been observed previously for $SrTiO_3$[93] and for Fe^{2+} states in hematite.[94]

4. CONCLUSIONS

An in-depth study of a deep eutectic solvent (DES)-involved precipitation route was conducted within the ZnO-V_2O_5 system. The precipitate consisting of $Zn_3(OH)_2V_2O_7 \cdot nH_2O$ and $Zn_5(OH)_6(CO_3)_2$ was obtained simply upon addition of the antisolvent DI H_2O to the precursor solution. We determined what synthetic parameters control size/morphology of the precipitate, i.e., temperature of the antisolvent and its addition rate. The low-temperature of antisolvent causes a lateral growth of individual 2D nanosheets ranging up to ~2 μm. The formation mechanism of a unique flower-like agglomerate is identified by the slow antisolvent addition rate. It is revealed that the layered structure of $Zn_3(OH)_2V_2O_7 \cdot nH_2O$ can host extra molecular species as well as varying amounts of H_2O depending on the synthetic conditions. Two zinc-rich vanadium oxides ZnO/$Zn_3V_2O_8$ and $Zn_4V_2O_9$ are prepared by a heat treatment of the precipitates. The phase evolution is understood by the similarity in crystal structures of zinc hydroxy vanadate hydrate and zinc-rich vanadates. The outstanding improvement of solid-state diffusion between ZnO and $Zn_3V_2O_8$ was achieved by their intimate mixing, producing the metastable $Zn_4V_2O_9$ within 30 s of annealing. We confirmed that the bond stretching mode of $[VO_4]^{3-}$ in the Raman spectrum of $Zn_4V_2O_9$ is split in the wavenumber range of 748−952 cm^{-1} due to four crystallographically independent vanadium sites. The most zinc-rich vanadate exhibits an indirect optical band gap of 2.94 eV with the absorption tail in 2.25−2.94 eV, which is ascribed to V^{4+} ions created because of oxygen vacancies. The surface photovoltage spectra confirm the 2.95 band gap and suggest an n-type character for $Zn_4V_2O_9$ based on the negative photovoltage signal. The photoluminescence experiment on $Zn_4V_2O_9$ reveals that the reduced vanadium cation acts as an inhibitor in yellow emission by decreasing an electron charge transfer in the VO_4 tetrahedra.

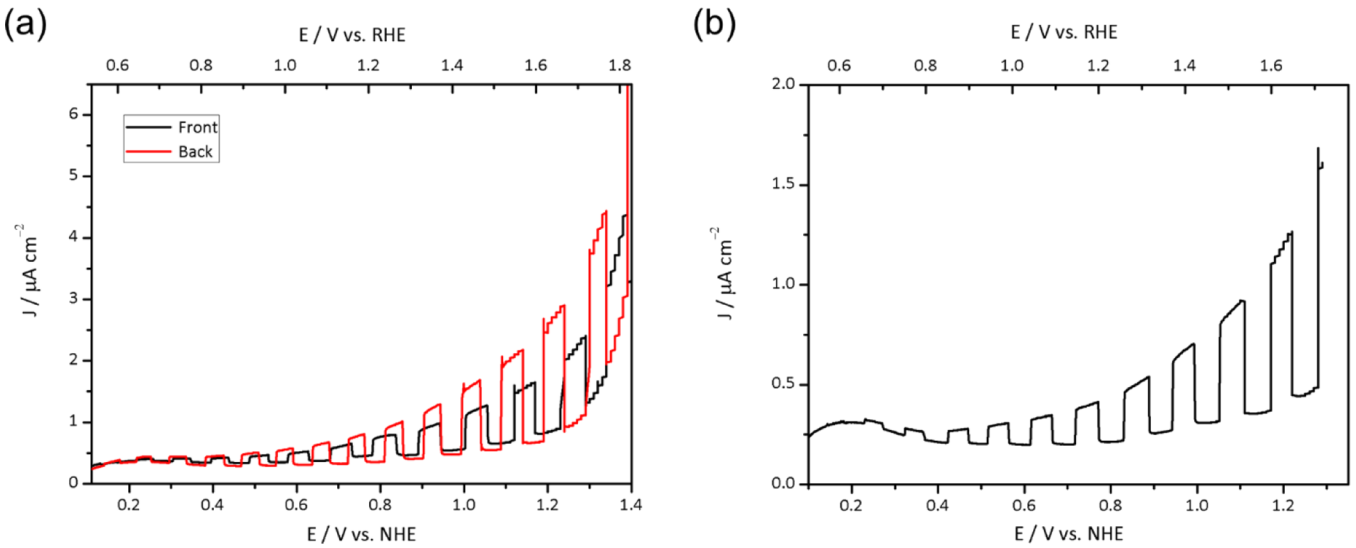

Figure 12. Photoelectrochemical scans of $Zn_4V_2O_9$ on FTO with intermitted illumination from a Xe lamp (100 $mW \cdot cm^{-2}$). The electrolytes are (a) degassed aqueous 0.1 M Na_2SO_4 (pH 7) containing 20% (v/v) methanol or (b) 0.1 M K_2SO_4 aqueous solution (pH 7).

https://doi.org/10.1021/acs.inorgchem.1c02511
Inorg. Chem. 2022, 61, 154−169

Photoelectrochemical (PEC) experiments reveal some activity of vanadate for water and methanol oxidation, when the applied potential is over 0.6 and 0.15 V vs NHE, respectively. However, the photocurrents are small and limited by the high concentration of V^{4+} defects, which function as electron−hole recombination sites. Overall, this work demonstrates versatility of DES as a reaction medium in preparation of semiconducting ternary metal oxides and potentially enables other metastable oxides.

■ ASSOCIATED CONTENT

Supporting Information

The Supporting Information is available free of charge at https://pubs.acs.org/doi/10.1021/acs.inorgchem.1c02511.

Additional PXRD patterns, SEM images, EDX elemental maps, Raman, FTIR, and XPS spectra, and optical micrograph and photo of the $Zn_4V_2O_9$ films (PDF)

■ AUTHOR INFORMATION

Corresponding Author

Julia V. Zaikina − *Department of Chemistry, Iowa State University, Ames, Iowa 50011, United States;* orcid.org/0000-0002-8755-1926; Email: yzaikina@iastate.edu

Authors

Sangki Hong − *Department of Chemistry, Iowa State University, Ames, Iowa 50011, United States*

Ye Cheng − *Department of Chemistry, University of California at Davis, Davis, California 95616, United States*

Shruti Hariyani − *Department of Chemistry, University of Houston, Houston, Texas 77204, United States; Texas Center for Superconductivity, University of Houston, Houston, Texas 77204, United States*

Jingzhe Li − *Department of Chemistry, Iowa State University, Ames, Iowa 50011, United States; U.S. Department of Energy, Ames Laboratory, Ames, Iowa 50011, United States;* orcid.org/0000-0002-1856-1477

Rachel M. Doughty − *Department of Chemistry, University of California at Davis, Davis, California 95616, United States;* Present Address: Department of Chemistry, Lawrence University, Appleton, Wisconsin 54911, United States

Aishwarya Mantravadi − *Department of Chemistry, Iowa State University, Ames, Iowa 50011, United States*

Adedoyin N. Adeyemi − *Department of Chemistry, Iowa State University, Ames, Iowa 50011, United States*

Emily A. Smith − *Department of Chemistry, Iowa State University, Ames, Iowa 50011, United States; U.S. Department of Energy, Ames Laboratory, Ames, Iowa 50011, United States;* orcid.org/0000-0001-7438-7808

Jakoah Brgoch − *Department of Chemistry, University of Houston, Houston, Texas 77204, United States; Texas Center for Superconductivity, University of Houston, Houston, Texas 77204, United States;* orcid.org/0000-0002-1406-1352

Frank E. Osterloh − *Department of Chemistry, University of California at Davis, Davis, California 95616, United States;* orcid.org/0000-0002-9288-3407

Complete contact information is available at: https://pubs.acs.org/10.1021/acs.inorgchem.1c02511

Notes

The authors declare no competing financial interest.

■ ACKNOWLEDGMENTS

We thank Dr. Kirill Kovnir and Dr. Javier Vela (Department of Chemistry, Iowa State University, and Ames Laboratory) for the access to the PXRD diffractometer and UV−vis spectrometer, respectively; Dr. Warren Straszheim (Materials Analysis Research Laboratory, Iowa State University) for the help with SEM/EDS measurement; Dr. Dapeng Jing (Materials Analysis Research Laboratory, Iowa State University) for the assistance with XPS data acquisition; Dr. Brett Boote (Chemical Instrument Services, Department of Chemistry, Iowa State University) for fruitful discussions and help with FTIR data collection; Dr. Wenqian Xu and Dr. Andrey Yakovenko at the 17-BM beamline, APS ANL; and Dr. Volodymyr Gvozdetskyi, Dr. Colin Harmer, and Gourab Bhaskar at Iowa State University for the assistance with HT-PXRD experiments. The financial support from the Iowa State University is gratefully acknowledged. The use of the Advanced Photon Source at Argonne National Laboratory was supported by the U.S. Department of Energy, Office of Science, Office of Basic Energy Sciences, under contract no. DE-AC02-06CH11357. Support for surface photovoltage spectroscopy measurements was provided by the U.S. Department of Energy, Office of Science, Office of Basic Energy Sciences, under award number DOE-SC0015329. S. Hariyani and J.B. would like to thank the National Science Foundation (CER-1911311) and the Welch Foundation (E-1981) for supporting this work. This research used the Opuntia/Sabine/Carya cluster(s) operated by the Research Computing Data Core at the University of Houston.

■ REFERENCES

(1) Kirklin, S.; Saal, J. E.; Meredig, B.; Thompson, A.; Doak, J. W.; Aykol, M.; Rühl, S.; Wolverton, C. The Open Quantum Materials Database (OQMD): assessing the accuracy of DFT formation energies. *npj Comput. Mater.* **2015**, *1*, 15010.

(2) Bergerhoff, G.; Hundt, R.; Sievers, R.; Brown, I. D. The inorganic crystal structure data base. *J. Chem. Inf. Model.* **1983**, *23*, 66−69.

(3) Karlsruhe, F. *Inorganic Crystal Structure Database*; http://icsd.fiz-karlsruhe.de/icsd/

(4) Lotfi, S.; Brgoch, J. Discovering Intermetallics Through Synthesis, Computation, and Data-Driven Analysis. *Chem. − Eur. J.* **2020**, *26*, 8689−8697.

(5) Aykol, M.; Dwaraknath, S. S.; Sun, W.; Persson, K. A. Thermodynamic limit for synthesis of metastable inorganic materials. *Sci. Adv.* **2018**, *4*, No. eaaq0148.

(6) Bartel, C. J.; Millican, S. L.; Deml, A. M.; Rumptz, J. R.; Tumas, W.; Weimer, A. W.; Lany, S.; Stevanovic, V.; Musgrave, C. B.; Holder, A. M. Physical descriptor for the Gibbs energy of inorganic crystalline solids and temperature-dependent materials chemistry. *Nat. Commun.* **2018**, *9*, 4168.

(7) Montanari, E.; Righi, L.; Calestani, G.; Migliori, A.; Gilioli, E.; Bolzoni, F. Room Temperature Polymorphism in Metastable $BiMnO_3$ Prepared by High-Pressure Synthesis. *Chem. Mater.* **2005**, *17*, 1765−1773.

(8) Omata, T.; Nagatani, H.; Suzuki, I.; Kita, M.; Yanagi, H.; Ohashi, N. Wurtzite $CuGaO_2$: A New Direct and Narrow Band Gap Oxide Semiconductor Applicable as a Solar Cell Absorber. *J. Am. Chem. Soc.* **2014**, *136*, 3378−3381.

(9) Jiang, Z.; Tian, S.; Lai, S.; McAuliffe, R.; Rogers, S. P.; Shim, M.; Shoemaker, D. P. Capturing phase evolution during solvothermal synthesis of metastable Cu_4O_3. *Chem. Mater.* **2016**, *28*, 3080−3089.

(10) O'Donnell, S.; Chung, C.-C.; Carbone, A.; Broughton, R.; Jones, J. L.; Maggard, P. A. Pushing the Limits of Metastability in

Semiconducting Perovskite Oxides for Visible-Light-Driven Water Oxidation. *Chem. Mater.* **2020**, 3054−3064.
(11) Song, J.; Ni, X.; Gao, L.; Zheng, H. Synthesis of metastable h-MoO_3 by simple chemical precipitation. *Mater. Chem. Phys.* **2007**, *102*, 245−248.
(12) Bose, A. C.; Ramamoorthy, R.; Ramasamy, S. Formability of metastable tetragonal solid solution in nanocrystalline NiO−ZrO powders. *Mater. Lett.* **2000**, *44*, 203−207.
(13) Ahn, T.; Kim, J. H.; Yang, H.-M.; Lee, J. W.; Kim, J.-D. Formation Pathways of Magnetite Nanoparticles by Coprecipitation Method. *J. Phys. Chem. C* **2012**, *116*, 6069−6076.
(14) Abellán, G.; Coronado, E.; Martí-Gastaldo, C.; Ribera, A.; Sánchez-Royo, J. F. Layered double hydroxide (LDH)−organic hybrids as precursors for low-temperature chemical synthesis of carbon nanoforms. *Chem. Sci.* **2012**, *3*, 1481−1485.
(15) Lenders, J. J. M.; Mirabello, G.; Sommerdijk, N. A. J. M. Bioinspired magnetite synthesis *via* solid precursor phases. *Chem. Sci.* **2016**, *7*, 5624−5634.
(16) Abbott, A. P.; Boothby, D.; Capper, G.; Davies, D. L.; Rasheed, R. K. Deep Eutectic Solvents Formed between Choline Chloride and Carboxylic Acids: Versatile Alternatives to Ionic Liquids. *J. Am. Chem. Soc.* **2004**, *126*, 9142−9147.
(17) Smith, E. L.; Abbott, A. P.; Ryder, K. S. Deep Eutectic Solvents (DESs) and Their Applications. *Chem. Rev.* **2014**, *114*, 11060−11082.
(18) Ciocirlan, O.; Iulian, O.; Croitoru, O. Effect of Temperature on the Physico-chemical Properties of Three Ionic Liquids Containing Choline Chloride. *Rev. Chim.* **2010**, *61*, 721−723.
(19) Hansen, B. B.; Spittle, S.; Chen, B.; Poe, D.; Zhang, Y.; Klein, J. M.; Horton, A.; Adhikari, L.; Zelovich, T.; Doherty, B. W.; Gurkan, B.; Maginn, E. J.; Ragauskas, A.; Dadmun, M.; Zawodzinski, T. A.; Baker, G. A.; Tuckerman, M. E.; Savinell, R. F.; Sangoro, J. R. Deep Eutectic Solvents: A Review of Fundamentals and Applications. *Chem. Rev.* **2021**, *121*, 1232−1285.
(20) Boston, R.; Foeller, P. Y.; Sinclair, D. C.; Reaney, I. M. Synthesis of Barium Titanate Using Deep Eutectic Solvents. *Inorg. Chem.* **2017**, *56*, 542−547.
(21) Söldner, A.; Zach, J.; Iwanow, M.; Gartner, T.; Schlosser, M.; Pfitzner, A.; König, B. Preparation of Magnesium, Cobalt and Nickel Ferrite Nanoparticles from Metal Oxides using Deep Eutectic Solvents. *Chem. − Eur. J.* **2016**, *22*, 13108−13113.
(22) Thorat, G. M.; Jadhav, H. S.; Roy, A.; Chung, W.-J.; Seo, J. G. Dual Role of Deep Eutectic Solvent as a Solvent and Template for the Synthesis of Octahedral Cobalt Vanadate for an Oxygen Evolution Reaction. *ACS Sustainable Chem. Eng.* **2018**, *6*, 16255−16266.
(23) Hong, S.; Doughty, R. M.; Osterloh, F. E.; Zaikina, J. V. Deep eutectic solvent route synthesis of zinc and copper vanadate n-type semiconductors - mapping oxygen vacancies and their effect on photovoltage. *J. Mater. Chem. A* **2019**, *7*, 12303−12316.
(24) Hong, A.; Burkhow, S. J.; Doughty, R. M.; Cheng, Y.; Ryan, B. J.; Mantravadi, A.; Roling, L. T.; Panthani, M. G.; Osterloh, F. E.; Smith, E. A.; Zaikina, J. V. Local Structural Disorder in Metavanadates MV_2O_6 (M = Zn and Cu) Synthesized by the Deep Eutectic Solvent Route: Photoactive Oxides with Oxygen Vacancies. *Chem. Mater.* **2021**, *33*, 1667−1682.
(25) Baby, J. N.; Sriram, B.; Wang, S. -F.; George, M. Effect of Various Deep Eutectic Solvents on the Sustainable Synthesis of $MgFe_2O_4$ Nanoparticles for Simultaneous Electrochemical Determination of Nitrofurantoin and 4-Nitrophenol. *ACS Sustainable Chem. Eng.* **2020**, *8*, 1479−1486.
(26) Datta, S.; Jo, C.; De Volder, M.; Torrente-Murciano, L. Morphological Control of Nanostructured V_2O_5 by Deep Eutectic Solvents. *ACS Appl. Mater. Interfaces* **2020**, *12*, 18803−18812.
(27) Baby, J. N.; Sriram, B.; Wang, S. -F.; George, M.; Govindasamy, M.; Joseph, X. B. Deep eutectic solvent-based manganese molybdate nanosheets for sensitive and simultaneous detection of human lethal compounds: comparing the electrochemical performances of M-molybdate (M = Mg, Fe, and Mn) electrocatalysts. *Nanoscale* **2020**, *12*, 19719.
(28) Dong, J.-Y.; Hsu, Y.-J.; Wong, D. S.-H.; Lu, S.-Y. Growth of ZnO Nanostructures with Controllable Morphology Using a Facile Green Antisolvent Method. *J. Phys. Chem. C* **2010**, *114*, 8867−8872.
(29) Dong, J.-Y.; Lin, W.-H.; Hsu, Y.-J.; Wong, D. S.-H.; Lu, S.-Y. Ultrafast formation of ZnO mesocrystals with excellent photocatalytic activities by a facile Tris-assisted antisolvent process. *CrystEngComm* **2011**, *13*, 6218.
(30) Dong, J.-Y.; Lin, C.-H.; Hsu, Y.-J.; Lu, S.-Y.; Wong, D. S.-H. Single-crystalline mesoporous ZnO nanosheets prepared with a green antisolvent method exhibiting excellent photocatalytic efficiencies. *CrystEngComm* **2012**, *14*, 4732−4737.
(31) Lu, Y.-H.; Lin, W.-H.; Yang, C.-Y.; Chiu, Y.-H.; Pu, Y.-C.; Lee, M.-H.; Tseng, Y.-C.; Hsu, Y.-J. A facile green antisolvent approach to Cu^{2+}-doped ZnO nanocrystals with visible-light-responsive photoactivities. *Nanoscale* **2014**, *6*, 8796.
(32) Yu, Y.; Niu, C.; Han, C.; Zhao, K.; Meng, J.; Xu, X.; Zhang, P.; Wang, L.; Wu, Y.; Mai, L. Zinc Pyrovanadate Nanoplates Embedded in Graphene Networks with Enhanced Electrochemical Performance. *Ind. Eng. Chem. Res.* **2016**, *55*, 2992−2999.
(33) Yan, H.; Luo, Y.; Xu, X.; He, L.; Tan, J.; Li, Z.; Hong, X.; He, P.; Mai, L. Facile and Scalable Synthesis of $Zn_3V_2O_7(OH)_2{\cdot}2H_2O$ Microflowers as a High-Performance Anode for Lithium-Ion Batteries. *ACS Appl. Mater. Interfaces* **2017**, *9*, 27707−27714.
(34) Gan, L. -H.; Deng, D.; Zhang, Y.; Li, G.; Wang, X.; Jiang, L.; Wang, C. -R. $Zn_3V_2O_8$ hexagon nanosheets: a high-performance anode material for lithium-ion batteries. *J. Mater. Chem. A* **2014**, *2*, 2461−2466.
(35) Wang, D.; Tang, J.; Zou, Z.; Ye, J. Photophysical and Photocatalytic Properties of a New Series of Visible-Light-Driven Photocatalysts $M_3V_2O_8$ (M = Mg, Ni, Zn). *Chem. Mater.* **2005**, *17*, 5177−5182.
(36) Nakajima, T.; Isobe, M.; Tsuchiya, T.; Ueda, Y.; Kumagai, T. A revisit of photoluminescence property for vanadate oxides AVO_3 (A: K, Rb and Cs) and $M_3V_2O_8$ (M: Mg and Zn). *J. Lumin.* **2009**, *129*, 1598−1601.
(37) Nakajima, T.; Isobe, M.; Tsuchiya, T.; Ueda, Y.; Manabe, T. Correlation between Luminescence Quantum Efficiency and Structural Properties of Vanadate Phosphors with Chained, Dimerized, and Isolated VO_4 Tetrahedra. *J. Phys. Chem. C* **2010**, *114*, 5160−5167.
(38) Dang, P.; Liu, D.; Wei, Y.; Li, G.; Lian, H.; Shang, M.; Lin, J. Highly Efficient Cyan-Green Emission in Self-Activated $Rb_3RV_2O_8$ (R = Y, Lu) Vanadate Phosphors for Full-Spectrum White Light-Emitting Diodes (LEDs). *Inorg. Chem.* **2020**, *59*, 6026−6038.
(39) Qian, T.; Fan, B.; Wang, H.; Zhu, S. Structure and luminescence properties of $Zn_3V_2O_8$ yellow phosphor for white light emitting diodes. *Chem. Phys. Lett.* **2019**, *715*, 34−39.
(40) Mordkovich, V. Z.; Hayashi, H.; Haemori, M.; Fukumura, T.; Kawasaki, M. Discovery and Optimization of New ZnO-Based Phosphors Using a Combinatorial Method. *Adv. Funct. Mater.* **2003**, *13*, 519−524.
(41) Kudo, A.; Omori, K.; Kato, H. A Novel Aqueous Process for Preparation of Crystal Form-Controlled and Highly Crystalline $BiVO_4$ Powder from Layered Vanadates at Room Temperature and Its Photocatalytic and Photophysical Properties. *J. Am. Chem. Soc.* **1999**, *121*, 11459−11467.
(42) Yan, Q.; Li, G.; Newhouse, P. F.; Yu, J.; Persson, K. A.; Gregoire, J. M.; Neaton, J. B. $Mn_2V_2O_7$: An Earth Abundant Light Absorber for Solar Water Splitting. *Adv. Energy Mater.* **2015**, *5*, 1401840.
(43) Zhang, J.; Wang, T.; Chang, X.; Li, A.; Gong, J. Fabrication of porous nanoflake $BiMO_x$ (M = W, V, and Mo) photoanodes *via* hydrothermal anion exchange. *Chem. Sci.* **2016**, *7*, 6381−6386.
(44) *PDXL: Integrated X-ray powder diffraction software*, Version 2.8.1.1; Rigaku: 2018.
(45) Chupas, P. J.; Chapman, K. W.; Kurtz, C.; Hanson, J. C.; Lee, P. L.; Grey, C. P. A versatile sample-environment cell for non-ambient X-ray scattering experiments. *J. Appl. Crystallogr.* **2008**, *41*, 822−824.

https://doi.org/10.1021/acs.inorgchem.1c02511
Inorg. Chem. 2022, 61, 154−169

(46) Toby, B. H.; Von Dreele, R. B. GSAS-II: the genesis of a modern open-source all purpose crystallography software package. *J. Appl. Crystallogr.* **2013**, *46*, 544−549.
(47) Kresse, G.; Furthmüller, J. Efficient iterative schemes for ab initio total-energy calculations using a plane-wave basis set. *Phys. Rev. B: Condens. Matter Mater. Phys.* **1996**, *54*, 11169−11186.
(48) Blöchl, P. E. Projector augmented-wave method. *Phys. Rev. B: Condens. Matter Mater. Phys.* **1994**, *50*, 17953−17979.
(49) Heyd, J.; Scuseria, G. E.; Ernzerhof, M. Hybrid functionals based on a screened Coulomb potential. *J. Chem. Phys.* **2003**, *118*, 8207−8215.
(50) Monkhorst, H. J.; Pack, J. D. Special points for Brillouin-zone integrations. *Phys. Rev. B: Condens. Matter Mater. Phys.* **1976**, *13*, 5188−5192.
(51) Parlinski, K.; Li, Z. Q.; Kawazoe, Y. First-principles determination of the soft mode in cubic ZrO_2. *Phys. Rev. Lett.* **1997**, *78*, 4063−4066.
(52) Fonari, A.; Stauffer, S. *Vasp_raman.Py*. 2013. https://github.com/raman-sc/VASP/.
(53) Kodera, M.; Wang, J.; Nail, B. A.; Liu, J.; Urabe, H.; Hisatomi, T.; Katayama, M.; Minegishi, T.; Osterloh, F. E.; Domen, K. Investigation of charge separation in particulate oxysulfide and oxynitride photoelectrodes by surface photovoltage spectroscopy. *Chem. Phys. Lett.* **2017**, *683*, 140−144.
(54) Zavalij, P. Y.; Zhang, F.; Whittingham, M. S. A New Zinc Pyrovanadate, $Zn_3(OH)_2V_2O_7{\cdot}2H_2O$, from X-ray Powder Data. *Acta Cryst.* **1997**, *CS3*, 1738−1739.
(55) Chirayil, T.; Zavalij, P. Y.; Whittingham, M. S. Hydrothermal Synthesis of Vanadium Oxides. *Chem. Mater.* **1998**, *10*, 2629−2640.
(56) Zavalij, P. Y.; Zhang, F.; Whittingham, M. S. The zinc−vanadium−oxygen−water system: hydrothermal synthesis and characterization. *Solid State Sci.* **2002**, *4*, 591−597.
(57) Gopal, R.; Calvo, C. Crystal Structure of α-$Zn_3(VO_4)_2$. *Can. J. Chem.* **1971**, *49*, 3056−3059.
(58) Waburg, M.; Müller-Buschbaum, H. Ein neues metastabiles Zinkoxovanadat: $Zn_4V_2O_9$. *Monatsh. Chem.* **1986**, *117*, 131−138.
(59) Abbott, A. P.; Capper, G.; Davies, D. L.; McKenzie, K. J.; Obi, S. U. Solubility of Metal Oxides in Deep Eutectic Solvents Based on Choline Chloride. *J. Chem. Eng. Data* **2006**, *51*, 1280−1282.
(60) Nagy, Z. K.; Fujiwara, M.; Woo, X. Y.; Braatz, R. D. Determination of the Kinetic Parameters for the Crystallization of Paracetamol from Water Using Metastable Zone Width Experiments. *Ind. Eng. Chem. Res.* **2008**, *47*, 1245−1252.
(61) Kim, K. J.; Mersmann, A. Estimation of metastable zone width in different nucleation processes. *Chem. Eng. Sci.* **2001**, *56*, 2315−2324.
(62) Sangwal, K. A novel self-consistent Nyvlt-like equation for metastable zone width determined by the polythermal method. *Cryst. Res. Technol.* **2009**, *44*, 231−247.
(63) Laird, A.; Chougule, M.; Hamad, M.; Morris, K. Thermodynamics Associated with Monitoring Pre-nucleation Aggregation at High Supersaturation. *Int. J. Pharm. Sci. Rev. Res.* **2013**, *18*, 6−12.
(64) Clark, M. D.; Morris, K. R.; Tomassone, M. S. Correlation of Solubility with the Metastable Limit of Nucleation Using Gauge-Cell Monte Carlo Simulations. *Langmuir* **2017**, *33*, 9081−9090.
(65) Shi, R.; Wang, Y.; Zhou, F.; Zhu, Y. $Zn_3V_2O_7(OH)_2(H_2O)_2$ and $Zn_3V_2O_8$ nanostructures: controlled fabrication and photocatalytic performance. *J. Mater. Chem.* **2011**, *21*, 6313−6320.
(66) Xia, C.; Guo, J.; Lei, Y.; Liang, H.; Zhao, C.; Alshareef, H. N. Rechargeable Aqueous Zinc-Ion Battery Based on Porous Framework Zinc Pyrovanadate Intercalation Cathode. *Adv. Mater.* **2018**, *30*, 1705580.
(67) Li, Y.; Teng, Y.; Zhang, Z.; Feng, Y.; Xue, P.; Tong, W.; Liu, X. Microwave-assisted synthesis of novel nanostructured $Zn_3(OH)_2V_2O_7{\cdot}2H_2O$ and $Zn_2V_2O_7$ as electrode materials for supercapacitors. *New J. Chem.* **2017**, *41*, 15298−15304.
(68) Iablokov, V.; Beaumont, S. K.; Alayoglu, S.; Pushkarev, V. V.; Specht, C.; Gao, J.; Alivisatos, A. P.; Kruse, N.; Somorjai, G. A. Size-Controlled Model Co Nanoparticle Catalysts for CO_2 Hydrogenation: Synthesis, Characterization, and Catalytic Reactions. *Nano Lett.* **2012**, *12*, 3091−3096.
(69) Yao, Y. F. Y.; Kummer, J. T. Ion exchange properties of and rates of ionic diffusion in beta-alumina. *J. Inorg. Nucl. Chem.* **1967**, *29*, 2453−2466.
(70) Chowdhury, M. T.; Takekawa, R.; Iwai, Y.; Kuwata, N.; Kawamura, J. Lithium ion diffusion in Li β-alumina single crystals measured by pulsed field gradient NMR spectroscopy. *J. Chem. Phys.* **2014**, *140*, 124509.
(71) Zhao, C.; Liu, L.; Qi, X.; Lu, Y.; Wu, F.; Zhao, J.; Yu, Y.; Hu, Y. -S.; Chen, L. Solid-State Sodium Batteries. *Adv. Energy Mater.* **2018**, *8*, 1703012.
(72) Shukla, A. K.; Ercius, P.; Gautam, A. R. S.; Cabana, J.; Dahmen, U. Electron Tomography Analysis of Reaction Path during Formation of Nanoporous NiO by Solid State Decomposition. *Cryst. Growth Des.* **2014**, *14*, 2453−2459.
(73) Dehmen, U.; Kim, M. G.; Searcy, A. W. Microstructural evolution during the decomposition of $Mg(OH)_2$. *Ultramicroscopy* **1987**, *23*, 365−370.
(74) Van Aken, P. A.; Langenhorst, F. Nanocrystalline, porous periclase aggregates as product of brucite dehydration. *Eur. J. Mineral.* **2001**, *13*, 329−341.
(75) Kurzawa, M.; Rychlowska-Himmel, I.; Bosacka, M.; Blonska-Tabero, A. Reinvestigation of Phase Equilibria in the V_2O_5−ZnO System. *J. Therm. Anal. Calorim.* **2001**, *64*, 1113−1119.
(76) Sinhamahapatra, A.; Giri, A. K.; Pal, P.; Pahari, S. K.; Bajaj, H. C.; Panda, A. B. A rapid and green synthetic approach for hierarchically assembled porous ZnO nanoflakes with enhanced catalytic activity. *J. Mater. Chem.* **2012**, *22*, 17227−17235.
(77) Chen, X.; Chen, D.; Lv, P.; Yan, F.; Zhan, Z.; Li, B.; Huang, F.; Liang, J. Subsolidus phase relationships in the system ZnO−V_2O_5−WO_3 research on suitable flux for ZnO crystal growth. *J. Alloys Compd.* **2009**, *476*, 241−244.
(78) Rychlowska-Himmel, I.; Blonska-Tabero, A. Synthesis and Thermal Stability of $Zn_4V_2O_9$. *J. Therm. Anal. Calorim.* **2001**, *64*, 1121−1125.
(79) Yang, L.; Tang, Y.; Tong, L.; Zhou, H.; Ding, J.; Fan, T.; Zhang, D. Efficient visible light photocatalytic water oxidation on $Zn_3(OH)_2V_2O_7{\cdot}2H_2O$ nanoplates: Effects of exposed facet and local crystal structure distortion. *Appl. Surf. Sci.* **2015**, *346*, 115−123.
(80) Frost, R. L.; Palmer, S. J.; Čejka, J.; Sejkora, J.; Plášil, J.; Bahfenne, S.; Keeffe, E. C. A Raman spectroscopic study of the different vanadate groups in solid-state compounds − model case: mineral phases vésigniéite $[BaCu_3(VO_4)_2(OH)_2]$ and volborthite $[Cu_3V_2O_7(OH)_2{\cdot}2H_2O]$. *J. Raman Spectrosc.* **2011**, *42*, 1701−1710.
(81) Hales, M. C.; Frost, R. L. Thermal Analysis of Smithsonite and Hydrozincite. *J. Therm. Anal. Calorim.* **2008**, *91*, 855−860.
(82) Zallen, R. *The Physics of Amorphous Solids*. Wiley: New York, 1983.
(83) Smith, J. E., Jr.; Brodsky, M. H.; Crowder, B. L.; Nathan, M. I.; Pinczuk, A. Raman Spectra of Amorphous Si and Related Tetrahedrally Bonded Semiconductors. *Phys. Rev. Lett.* **1971**, *26*, 642−646.
(84) Ni, S.; Wang, X.; Zhou, G.; Yang, F.; Wang, J.; He, D. Crystallized $Zn_3(VO_4)_2$: Synthesis, characterization and optical property. *J. Alloys Compd.* **2010**, *491*, 378−381.
(85) Unnimaya, A. N.; Suresh, E. K.; Ratheesh, R. Crystal structure and microwave dielectric properties of new alkaline earth vanadate $A_4V_2O_9$ (A = Ba, Sr, Ca, Mg and Zn) ceramics for LTCC applications. *Mater. Res. Bull.* **2017**, *88*, 174−181.
(86) Biesinger, M. C.; Lau, L. W.; Gerson, A. R.; Smart, R. S. C. Resolving surface chemical states in XPS analysis of first row transition metals, oxides and hydroxides: Sc, Ti, V, Cu and Zn. *Appl. Surf. Sci.* **2010**, *257*, 887−898.
(87) Biesinger, M. C.; Payne, B. P.; Lau, L. W. M.; Gerson, A.; Smart, R. S. C. X-ray photoelectron spectroscopic chemical state quantification of mixed nickel metal, oxide and hydroxide systems. *Surf. Interface Anal.* **2009**, *41*, 324−332.

https://doi.org/10.1021/acs.inorgchem.1c02511
Inorg. Chem. 2022, 61, 154−169

(88) Silversmit, G.; Depla, D.; Poelman, H.; Marin, G. B.; De Gryse, R. An XPS study on the surface reduction of V_2O_5(001) induced by Ar^+ ion bombardment. *Surf. Sci.* **2006**, *600*, 3512−3517.
(89) Kröger, F. A.; Vink, H. J. Relations between the Concentrations of Imperfections in Crystalline Solids. *Solid State Phys.* **1956**, *3*, 307−435.
(90) Dittrich, T.; Fengler, S. *Surface Photovoltage Analysis of Photoactive Materials*. World Scientific Publishing Europe Ltd.: London, 2020, p 287.
(91) Kronik, L.; Shapira, Y. Surface Photovoltage Spectroscopy of Semiconductor Structures: At the Crossroads of Physics, Chemistry and Electrical Engineering. *Surf. Interface Anal.* **2001**, *31*, 954−965.
(92) Liqiang, J.; Xiaojun, S.; Jing, S.; Weimin, C.; Zili, X.; Yaoguo, D.; Honggang, F. Review of surface photovoltage spectra of nano-sized semiconductor and its applications in heterogeneous photocatalysis. *Sol. Energy Mater. Sol. Cells* **2003**, *79*, 133−151.
(93) Zhao, Z.; Goncalves, R. V.; Barman, S. K.; Willard, E. J.; Byle, E.; Perry, R.; Wu, Z.; Huda, M. N.; Moulé, A. J.; Osterloh, F. E. Electronic structure basis for enhanced overall water splitting photocatalysis with aluminum doped $SrTiO_3$ in natural sunlight. *Energy Environ. Sci.* **2019**, *12*, 1385−1395.
(94) Lohaus, C.; Klein, A.; Jaegermann, W. Limitation of Fermi level shifts by polaron defect states in hematite photoelectrodes. *Nat. Commun.* **2018**, *9*, 4309.

https://doi.org/10.1021/acs.inorgchem.1c02511
Inorg. Chem. 2022, 61, 154−169